INTERNATIONAL CENTRE FOR THEORETICAL PHYSICS
I.C.T.P., P.O. BOX 586, 34100 TRIESTE, ITALY. CABLE: CENTRATOM TRIESTE

H4.SMR/782-2

Second Workshop on Three-Dimensional Modelling of Seismic Waves Generation, Propagation and their Inversion

7 - 18 November 1994

Earthquake Faulting: The Forward Problem

S. Das

University of Oxford
Department of Earth Sciences
United Kingdom

These lectures assume a knowledge of the Theory of Elasticity and some knowledge of seismology. A good mathematics background is essential.

The lecture notes for Lecture 1 are extracted from the following sources:

Aki, K. and P.G. Richards (1980) Quantitative Seismology: Theory and Methods. 932 pp., W.H. Freeman and Company, San Francisco, California, 1980.

Kostrov, B.V. and S. Das (1988) Principles of Earthquake Source Mechanics, Cambridge University Press, Applied Math. and Mech. Ser., Cambridge Univ. Press, N.Y., pp. 286, 1988.

Note: These notes are an attempt to provide a complete background to the lectures. Only some aspects will be discussed in the lectures. The reader is referred to the original sources for complete details and for references mentioned in the next pages.

EQUATIONS OF MOTION IN AN ELASTIC MEDIUM

(due to Navier)

The equation of motion in an elastic medium is given by

$$\tau_{ij,j} + f_i = \rho \ddot{u}_i \qquad \cdots (1)$$

where τ_{ij} is the stress tensor, $i, j, k, l = 1, 2, 3$ & $\tau_{ij} = \tau_{ji}$

$$= c_{ijkl}\, e_{kl} \qquad e_{kl} = \tfrac{1}{2}(u_{i,j} + u_{j,i})$$

where c's are the elastic constants; e_{ij} is the strain tensor;
u_i is the component of displacement in the i-direction
f_i " " " " body force " " "
ρ is the density and Einstein's summation convention for tensors is used (i.e. equation (1) is a set of 3 equations).

2.3 Theorems of Uniqueness and Reciprocity

It is natural to introduce the discussion of uniqueness (for the displacement field $\mathbf{u}$ throughout a body with volume V and surface S) with some general remarks concerning the ways in which motion can be set up. Because the displacement is constrained to satisfy (2.17) throughout V, the application of body forces will generate a displacement field, as will the application of tractions on the surface S. We shall show that specification of the body forces throughout V, and tractions over all of S, is enough to determine uniquely the displacement field that will develop throughout V from given initial conditions. An alternative way to specify the influence of S on the displacement field is to give a boundary condition for displacement itself (on S) instead of for the traction. For example, S might be rigid. It might seem at first that the traction on S and the displacement on S are independent properties of the displacement field throughout V. This is not so, however, and it is important for an intuitive understanding of Sections 2.3–2.5 to appreciate that traction over S determines the displacement over S, and vice versa.

UNIQUENESS THEOREM

The displacement $\mathbf{u} = \mathbf{u}(\mathbf{x}, t)$ throughout the volume V with surface S is uniquely determined after time t_0 by the initial values of displacement and particle velocity at t_0, throughout V; and by values at all times $t \geq t_0$ of (i) the body forces $\mathbf{f}$ and the heat $\mathcal{Q}$ supplied throughout V; (ii) the tractions $\mathbf{T}$ over any part S_1 of S; and (iii) the displacement over the remainder S_2 of S, with $S_1 + S_2 = S$. (Either of S_1 or S_2 can be the whole of S.)

PROOF

Suppose $\mathbf{u}_1$ and $\mathbf{u}_2$ are any solutions for $\mathbf{u}$ that satisfy the same initial conditions and are set up by the same values for (i)–(iii). Then the difference $\mathbf{U} \equiv \mathbf{u}_1 - \mathbf{u}_2$ is a displacement field having zero initial conditions, and is set up by zero body forces, zero heating, zero traction on S_1, and $\mathbf{U} = \mathbf{0}$ on S_2. It remains to prove that $\mathbf{U} = \mathbf{0}$ throughout V for $t > t_0$.

The rate of doing mechanical work in the displacement field $\mathbf{U}$ is clearly zero throughout V and S_1 and S_2 (see (2.22)) for $t \geq t_0$. The third equality in (2.22) can be integrated from t_0 to t, and, together with the zero initial conditions and the use of a strain-energy function ($\mathbf{U}$ involves adiabatic changes), it follows that

$$\iiint_V \frac{1}{2}\rho \dot{U}_i \dot{U}_i \, dV + \iiint_V \frac{1}{2} c_{ijkl} U_{i,j} U_{k,l} \, dV = 0.$$

Both the kinetic and strain energies are positive definite, so that $\dot{U}_i = 0$ for $t \geq t_0$. But $U_i = 0$ at $t = t_0$, and hence $\mathbf{U} = \mathbf{0}$ throughout V for $t \geq t_0$.

BOX **2.4**

Use of the term "homogeneous," as applied to equations and boundary conditions

The equation for elastic displacement is $\mathbf{L}(\mathbf{u}) = \mathbf{f}$, where $\mathbf{L}$ is the vector differential operator defined on the components of $\mathbf{u}$ by

$$(\mathbf{L}(\mathbf{u}))_i \equiv \rho \ddot{u}_i - (c_{ijkl} u_{k,l})_{,j}.$$

If body forces are absent, then the equation $\mathbf{L}(\mathbf{u}) = \mathbf{0}$ for $\mathbf{u}$ is said to be *homogeneous*. A *homogeneous boundary condition* on the surface S is one for which *either* the displacement *or* the traction vanishes at every point of the surface.

This terminology is reminiscent of linear algebra, for which a system of n equations in n unknowns, in the form $\mathbf{Ax} = \mathbf{0}$, is also said to be homogeneous. Here, $\mathbf{x}$ is a column vector and $\mathbf{A}$ is some $n \times n$ matrix. It is well known that nontrivial solutions ($\mathbf{x} \neq \mathbf{0}$) can exist, but only if $\mathbf{A}$ has a special property (namely, a zero determinant). The corresponding result in dynamic elasticity is that motions can occur throughout a finite elastic volume V without any body forces and with a homogeneous boundary condition over the surface of V. These are the *free oscillations* or *normal modes* of the body, which can occur only at certain frequencies. See Chapter 8.

RECIPROCITY THEOREMS

We shall state and prove several general relationships between a pair of solutions for the displacement through an elastic body V.

Suppose that $\mathbf{u} = \mathbf{u}(\mathbf{x}, t)$ is one of these displacement fields, and that $\mathbf{u}$ is due to body forces $\mathbf{f}$ and boundary conditions on S and initial conditions at time $t = 0$. Let $\mathbf{v} = \mathbf{v}(\mathbf{x}, t)$ be another displacement field due to body forces $\mathbf{g}$ and to boundary conditions and initial conditions (at $t = 0$) which in general are different from the conditions for $\mathbf{u}$. To distinguish the tractions on surfaces normal to $\mathbf{n}$ in these two cases, we shall use the notation $\mathbf{T}(\mathbf{u}, \mathbf{n})$ for the traction due to the displacement $\mathbf{u}$ and, similarly, $\mathbf{T}(\mathbf{v}, \mathbf{n})$ for the traction due to $\mathbf{v}$.

The first reciprocal relation to note between $\mathbf{u}$ and $\mathbf{v}$ is

IMPORTANT

$$\iiint_V (\mathbf{f} - \rho\ddot{\mathbf{u}}) \cdot \mathbf{v}\, dV + \iint_S \mathbf{T}(\mathbf{u}, \mathbf{n}) \cdot \mathbf{v}\, dS = \iiint_V (\mathbf{g} - \rho\ddot{\mathbf{v}}) \cdot \mathbf{u}\, dV + \iint_S \mathbf{T}(\mathbf{v}, \mathbf{n}) \cdot \mathbf{u}\, dS. \quad (2.34)$$

This result is due to Betti. It can easily be proved by subsitution from (2.17) and (2.16) and then applying the divergence theorem to reduce the left side to

BOX **2.5**

Parallels

A rearrangement of Betti's relation (2.34) gives

$$\iiint_V \{v_i(c_{ijkl}u_{k,l})_{,j} - u_i(c_{ijkl}v_{k,l})_{,j}\}\, dV = \iint_S \{v_i T_i(\mathbf{u}, \mathbf{n}) - u_i T_i(\mathbf{v}, \mathbf{n})\}\, dS.$$

This is a vector theorem for the second-order spatial derivatives occurring in the wave equation of elasticity, which is analogous to Green's theorem

$$\iiint_V (\psi \nabla^2 \phi - \phi \nabla^2 \psi)\, dV = \iint_S \left(\psi \frac{\partial \phi}{\partial n} - \phi \frac{\partial \psi}{\partial n}\right) dS$$

for scalars and the Laplacian operator. Green's theorem is a working tool for studying inhomogeneous equations, such as $\nabla^2 \phi = -4\pi\rho$, and we shall use Betti's theorem for the elastic wave equation, in which the inhomogeneity is the body-force term.

There are many further analogies between Dirichlet problems (for potentials that are zero on S) and elasticity problems with rigid boundaries; and between Neumann problems ($\partial\phi/\partial n = 0$ on S) and traction-free boundaries.

$\iiint_V c_{ijkl}v_{i,j}u_{k,l}\, dV$. Similarly, the right-hand side reduces to $\iiint_V c_{ijkl}u_{i,j}v_{k,l}\, dV$, and (2.34) follows from the symmetry $c_{ijkl} = c_{klij}$.

Note that Betti's theorem does not involve initial conditions for $\mathbf{u}$ or $\mathbf{v}$. Furthermore, it remains true even if the quantities $\mathbf{u}$, $\ddot{\mathbf{u}}$, $\mathbf{T}(\mathbf{u}, \mathbf{n})$, and $\mathbf{f}$ are evaluated at time t_1 but $\mathbf{v}$, $\ddot{\mathbf{v}}$, $T(\mathbf{v}, \mathbf{n})$, $\mathbf{g}$ are evaluated at a different time t_2. If we choose $t_1 = t$ and $t_2 = \tau - t$ and integrate (2.34) over the temporal range 0 to τ, then the acceleration terms reduce to terms that depend only on the initial and final values, since

$$\int_0^\tau \rho\{\ddot{\mathbf{u}}(t) \cdot \mathbf{v}(\tau - t) - \mathbf{u}(t) \cdot \ddot{\mathbf{v}}(\tau - t)\}\, dt$$

$$= \rho \int_0^\tau \frac{\partial}{\partial t} \{\dot{\mathbf{u}}(t) \cdot \mathbf{v}(\tau - t) + \mathbf{u}(t) \cdot \dot{\mathbf{v}}(\tau - t)\}\, dt$$

$$= \rho\{\dot{\mathbf{u}}(\tau) \cdot \mathbf{v}(0) - \dot{\mathbf{u}}(0) \cdot \mathbf{v}(\tau) + \mathbf{u}(\tau) \cdot \dot{\mathbf{v}}(0) - \mathbf{u}(0) \cdot \dot{\mathbf{v}}(\tau)$$

If there is some time τ_0 before which $\mathbf{u}$ and $\mathbf{v}$ are everywhere zero throughout V (and hence $\dot{\mathbf{u}} = \dot{\mathbf{v}} = \mathbf{0}$ for $\tau \leq \tau_0$), then the convolution

$$\int_{-\infty}^{\infty} \rho\{\ddot{\mathbf{u}}(t) \cdot \mathbf{v}(\tau - t) - \mathbf{u}(t) \cdot \ddot{\mathbf{v}}(\tau - t)\}\, dt$$

is zero. We deduce from Betti's theorem the important result, for displacement fields with a quiescent past, that

$$\int_{-\infty}^{\infty} dt \iiint_V \{\mathbf{u}(\mathbf{x}, t) \cdot \mathbf{g}(\mathbf{x}, \tau - t) - \mathbf{v}(\mathbf{x}, \tau - t) \cdot \mathbf{f}(\mathbf{x}, t)\}\, dV$$

$$= \int_{-\infty}^{\infty} dt \iint_S \{\mathbf{v}(\mathbf{x}, \tau - t) \cdot \mathbf{T}(\mathbf{u}(\mathbf{x}, t), \mathbf{n}) - \mathbf{u}(\mathbf{x}, t) \cdot \mathbf{T}(\mathbf{v}(\mathbf{x}, \tau - t), \mathbf{n})\}\, dS. \quad (2.35)$$

Green's function for elastodynamics

Green's functions are the impulse response of an elastic solid, that is, it is the displacement generated in the body by the application of an unit force $f_i = \delta(\bar{x})\,\delta(t)$ where $\bar{x} = (x_1, x_2, x_3)$ and t is the time.

2.4 Introducing Green's Function for Elastodynamics

A major aim of this chapter and the next is the development of a representation for the displacements that typically occur in seismology. The representation will be a formula for the displacement (at a general point in space and time) in terms of the quantities that originated the motion, and we have seen (in the uniqueness theorem) that these are body forces and applied tractions or displacements over the surface of the elastic body under discussion. For earthquake faulting, the seismic source is complicated in that it extends over a finite fault plane (or a finite volume) and over a finite amount of time, and in general involves motions (at the source) that have varying direction and magnitude. We shall find that the representation theorem is really nothing but a bookkeeping device by which the displacement from realistic source models is synthesized from the displacement produced by the simplest of sources—namely, the unidirectional unit impulse, which is localized precisely in both space and time.

The displacement field from such a simple source is the elastodynamic Green function. If the unit impulse is applied at $\mathbf{x} = \boldsymbol{\xi}$ and $t = \tau$ and in the n-direction (see (2.4), taking A = unit constant with dimensions of impulse), then we denote the ith component of displacement at general $(\mathbf{x}, t)$ by $\mathbf{G}_{in}(\mathbf{x}, t; \boldsymbol{\xi}, \tau)$. Clearly, this Green function is a tensor (we shall work throughout with Cartesian tensors, and therefore do not distinguish between tensors and dyadics). It depends on both receiver and source coordinates, and satisfies the equation

$$\rho \frac{\partial^2}{\partial t^2} G_{in} = \delta_{in}\delta(\mathbf{x} - \boldsymbol{\xi})\delta(t - \tau) + \frac{\partial}{\partial x_j}\left(c_{ijkl} \frac{\partial}{\partial x_l} G_{kn}\right) \tag{2.36}$$

throughout V. We shall invariably use the initial conditions that $\mathbf{G}(\mathbf{x}, t; \boldsymbol{\xi}, \tau)$ and $\partial\{\mathbf{G}(\mathbf{x}, t; \boldsymbol{\xi}, \tau)\}/\partial t$ are zero for $t \leq \tau$ and $\mathbf{x} \neq \boldsymbol{\xi}$. To specify $\mathbf{G}$ uniquely, it remains to state the boundary conditions on S, and we shall use a variety of different boundary conditions in different applications.

If the boundary conditions are independent of time (e.g., S always rigid), then the time origin can be shifted at will, and we see from (2.36) that $\mathbf{G}$ depends on t

and τ only via the combination $t - \tau$. Hence

$$\mathbf{G}(\mathbf{x}, t; \xi, \tau) = \mathbf{G}(\mathbf{x}, t - \tau; \xi, 0) = \mathbf{G}(\mathbf{x}, -\tau; \xi, -t), \tag{2.37}$$

which is a reciprocal relation for source and receiver times.

If $\mathbf{G}$ satisfies homogeneous boundary conditions on S, then (2.35) can be used to obtain an important reciprocal relation for source and receiver positions. One takes $\mathbf{f}$ to be a unit impulse applied in the m-direction at $\mathbf{x} = \xi_1$ and time $t = \tau_1$, and $\mathbf{g}$ to be a unit impulse applied in the n-direction at $\mathbf{x} = \xi_2$ and time $t = -\tau_2$. Then $u_i = G_{im}(\mathbf{x}, t; \xi_1, \tau_1)$ and $v_i = G_{in}(\mathbf{x}, t; \xi_2, -\tau_2)$, so that (2.35) directly yields

$$G_{nm}(\xi_2, \tau + \tau_2; \xi_1, \tau_1) = G_{mn}(\xi_1, \tau - \tau_1; \xi_2, -\tau_2). \tag{2.38}$$

Choosing $\tau_1 = \tau_2 = 0$, this becomes

$$G_{nm}(\xi_2, \tau; \xi_1, 0) = G_{mn}(\xi_1, \tau; \xi_2, 0), \tag{2.39}$$

which specifies a purely spatial reciprocity. Choosing $\tau = 0$ in (2.38) gives

$$G_{nm}(\xi_2, \tau_2; \xi_1, \tau_1) = G_{mn}(\xi_1, -\tau_1; \xi_2, -\tau_2), \tag{2.40}$$

which specifies a space-time reciprocity.

The actual computation of an elastodynamic Green function can itself be a complicated problem. We shall take up this subject in Chapter 4 for the simplest of elastic solids (homogeneous, isotropic, infinite) and also for the case of large separation between source and receiver in inhomogeneous media.

2.5 Representation Theorems

If the integrated form of Betti's theorem, our equation (2.35), is used with a Green function for one of the displacement fields, then a representation for the other displacement field becomes available.

Specifically, suppose we are interested in finding an expression for the displacement $\mathbf{u}$ due both to body forces $\mathbf{f}$ throughout V and to boundary conditions on S. We substitute into (2.35) the body force $g_i(\mathbf{x}, t) = \delta_{in}\delta(\mathbf{x} - \xi)\delta(t)$, for which the corresponding solution is $v_i(\mathbf{x}, t) = G_{in}(\mathbf{x}, t; \xi, 0)$, and find

$$\begin{aligned} u_n(\xi, \tau) = &\int_{-\infty}^{\infty} dt \iiint_V f_i(\mathbf{x}, t) G_{in}(\mathbf{x}, \tau - t; \xi, 0)\, dV \\ &+ \int_{-\infty}^{\infty} dt \iint_S \{G_{in}(\mathbf{x}, \tau - t; \xi, 0) T_i(\mathbf{u}(\mathbf{x}, t), \mathbf{n}) \\ &- u_i(\mathbf{x}, t) c_{ijkl} n_j G_{kn,l}(\mathbf{x}, \tau - t; \xi, 0)\}\, dS. \end{aligned}$$

Before giving a physical interpretation of this equation, it is helpful to interchange the symbols $\mathbf{x}$ and ξ and the symbols t and τ. This permits $(\mathbf{x}, t)$ to be the general position and time at which a displacement is to be evaluated, regarded as an integral over volume and surface elements at varying ξ with a temporal convolution. The result is

$$u_n(\mathbf{x}, t) = \int_{-\infty}^{\infty} d\tau \iiint_V f_i(\xi, \tau) G_{in}(\xi, t - \tau; \mathbf{x}, 0)\, dV(\xi) + \int_{-\infty}^{\infty} d\tau \iint_S \{G_{in}(\xi, t - \tau; \mathbf{x}, 0) T_i(\mathbf{u}(\xi, \tau), \mathbf{n}) - u_i(\xi, \tau) c_{ijkl}(\xi) n_j G_{kn,l}(\xi, t - \tau; \mathbf{x}, 0)\}\, dS(\xi). \tag{2.41}$$

This is our first representation theorem. It states a way in which displacement $\mathbf{u}$ at a certain point is made up from contributions due to the force $\mathbf{f}$ throughout V, plus contributions due to the traction $\mathbf{T}(\mathbf{u}, \mathbf{n})$ and the displacement $\mathbf{u}$ itself on S. However, the way in which each of these three contributions is weighted is unsatisfactory, since each involves a Green function with source at $\mathbf{x}$ and observation point at ξ. (Note that the last term in (2.41) involves differentiation with respect to ξ_l.) We want $\mathbf{x}$ to be the observation point, so that the total displacement obtained there can be regarded as the sum (integral) of contributing displacements at $\mathbf{x}$ due to each volume element and surface element. The reciprocal theorem for $\mathbf{G}$ must be invoked, but this will require extra conditions on Green's function itself, since the equation $G_{in}(\xi, t - \tau; \mathbf{x}, 0) = G_{ni}(\mathbf{x}, t - \tau; \xi, 0)$ (see (2.39)) was proved only if $\mathbf{G}$ satisfies homogeneous boundary conditions on S, whereas (2.41) is valid for *any* Green function set up by an impulsive force in the n-direction at $\xi = \mathbf{x}$ and $\tau = t$.

We shall examine two different cases. Suppose, first, that Green's function is determined with S as a rigid boundary. We write $\mathbf{G}^{\text{rigid}}$ for this function and $G_{in}^{\text{rigid}}(\xi, t - \tau; \mathbf{x}, 0) = 0$ for ξ in S. Then (2.41) becomes

$$u_n(\mathbf{x}, t) = \int_{-\infty}^{\infty} d\tau \iiint_V f_i(\xi, \tau) G_{ni}^{\text{rigid}}(\mathbf{x}, t - \tau; \xi, 0)\, dV - \int_{-\infty}^{\infty} d\tau \iint_S u_i(\xi, \tau) c_{ijkl} n_j \frac{\partial}{\partial \xi_l} G_{nk}^{\text{rigid}}(\mathbf{x}, t - \tau; \xi, 0)\, dS. \tag{2.42}$$

Alternatively, we can use $\mathbf{G}^{\text{free}}$ as Green's function, so that the traction $c_{ijkl} n_j (\partial/\partial \xi_l) G_{kn}^{\text{free}}(\xi, t - \tau; \mathbf{x}, 0)$ is zero for ξ in S, finding

$$u_n(\mathbf{x}, t) = \int_{-\infty}^{\infty} d\tau \iiint_V f_i(\xi, \tau) G_{ni}^{\text{free}}(\mathbf{x}, t - \tau; \xi, 0)\, dV + \int_{-\infty}^{\infty} d\tau \iint_S G_{ni}^{\text{free}}(\mathbf{x}, t - \tau; \xi, 0) T_i(\mathbf{u}(\xi, \tau), \mathbf{n})\, dS. \tag{2.43}$$

VERY IMPORTANT

Equations (2.41)–(2.43) are all different forms of the representation theorem, and each has its special uses. Taken together, they seem to imply a contradiction to the question of whether $\mathbf{u}(\mathbf{x}, t)$ depends upon displacement on S (see (2.42)) or traction (see (2.43)) or both (see (2.41)). But since traction and displacement cannot be specified independently on the surface of an elastic medium, there is no contradiction.

The surface on which values of traction (or displacement) are explicitly required has been taken, in this chapter, as external to the volume V. It is often useful to take this surface to include two adjacent internal surfaces, being the opposite faces of a buried fault. Specialized forms of the representation theorem can then be developed, which enable one to analyze the earthquakes set up by activity on a buried fault. This subject is central to earthquake source theory, and is taken up in the following chapter.

So far, we have considered only Cartesian coordinate systems. In practice, the seismologist is often required to use different coordinates that allow the physical relationship between components of displacement, stress, and strain to be simplified for the geometry of a particular problem. In particular, it is often found that a boundary condition must be applied on a surface that can be chosen as the surface on which a general curvilinear coordinate is constant. Vector operations grad, div, curl, and ∇^2 are derived for general orthogonal coordinates in many texts, but rather more is needed to analyze the vector operations required in elasticity.

Equation (2.42) and (2.43) are the most important for our purposes. If body forces are absent, then (2.42) + (2.43) become

$$u_n(\bar{x},t) = -\int_{-\infty}^{\infty} d\tau \iint_S u_i(\bar{\xi},\tau)\, c_{ijkl}\, n_j \frac{\partial}{\partial \xi_l} G_{nk}^{\text{rigid}}(\bar{x},t-\tau;\bar{\xi},0)\, dS$$

and

$$u_n(\bar{x},t) = \int_{-\infty}^{\infty} d\tau \iint_S G_{ni}^{\text{free}}(\bar{x},t-\tau;\bar{\xi},0)\, T_i\left(\bar{u}(\bar{\xi},\tau),\bar{n}\right) dS$$

When the first of these equations is used, ie. if the LHS is determined when u_i and G_{nk}^{rigid} are known, the problem is called the DISLOCATION model for the seismic source. i.e. given the displacements u_i on S we find the displacement at some point using this equation.

When the second of these equations is used, ie. the LHS is determined when G_{ni}^{free} and the stress T_i are given, the problem is called the CRACK model for the seismic source.

The "dislocation" model is a kinematic model whereas the "crack" model is a dynamic model.

BOX **5.3**

The distinction between kinematics and dynamics

Kinematics is the branch of mechanics that deals purely with motion, without analyzing the underlying forces that cause or participate in the motion. Dynamics is the branch of mechanics that deals directly with force systems, and with the energy balance that governs motion. From these fundamental definitions, two useful conventions have developed for applying the words "kinematic" and "dynamic."

First, in the analysis of displacements alone, kinematic properties are those that may be derived from the eikonal equation (4.41), whereas dynamic properties are those related to displacement amplitudes. Thus the existence of particular wavefronts and ray paths is part of the kinematics of the problem in hand. As an example of a dynamic problem, we might ask if a certain approximation is adequate for the displacements observed at a given receiver at some given distance from a localized source.

Second, in those problems in which we have a direct interest both in the displacement and the associated system of stresses, then kinematic properties are properties of the displacement field and dynamic properties are related to the stresses. For example, if the relative displacement between opposite faces of a fault surface is known as a function of space and time, we say that we have a kinematic description of the fault motion. If the stresses (i.e., traction components) are known on the fault surface, we have a dynamic description. As another example, one refers to boundary conditions as being kinematic or dynamic, in the sense developed in the present section.

FORWARD and INVERSE PROBLEMS.

Forward problems in mechanics are when the physical laws governing motion are given together with a system of forces acting on some body and we are required to find the resulting motion. In the earthquake problem, we may be given the material properties at the place in the earth's crust where rupture is occurring together with the equations of motion in an elastic body and we are required to find the motion on the fault.
Another forward problem is when the motion on the fault is determined, to calculate the ground motion at seismometers located all over the world.

Inverse problems are when the resulting motion due to a system of forces are known to determine the forces which caused the motion. In seismology, we measure the ground motion at seismic stations and reconstruct the motion at the hypocentre of the earthquake

∴ Forward problem → KNOWN cause; FIND effect
Inverse problem → KNOWN effect; FIND cause.

We shall consider inverse problems in the 3rd lecture.

INTERIOR CRACK PROBLEM

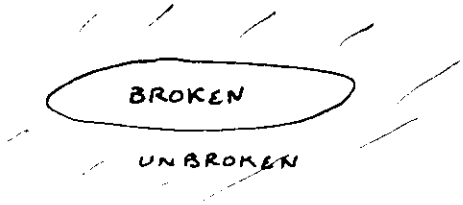

"CRACK" IN SEISMOLOGY

EXTERIOR CRACK PROBLEM

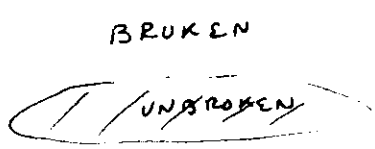

"ASPERITY" IN SEISMOLOGY

THE BOUNDARY-INTEGRAL EQUATION METHOD

5.1 Representation relations

In order to reduce the earthquake source problem to the solution of a boundary-integral equation, it is necessary first to represent the stress and displacement fields throughout the medium in terms of the displacement discontinuity or the traction perturbations on the fault plane. In the case of the kinematic description of the earthquake source ("dislocation" model), such representation relations provide an explicit solution, as we saw in Section 3.2. However, as we shall show later, the boundary conditions for the dynamically described source ("crack" model) are of mixed type, and such representation relations do not give the required solution explicitly; instead, they relate the boundary values of the traction perturbations and slip, neither of which are known on the entire boundary (fault plane). Together with boundary conditions, these relations comprise the integral equations. When these integral equations are solved, the displacement and stress fields inside the body can be obtained using the same representation relations.

The geometry of the problem is shown in Figure 5.1. The plane $X_3 = 0$ is taken as the crack plane and denoted by S. Let $S(t)$ be that portion of the $X_3 = 0$ plane where slip is nonvanishing at time t and let $\bar{S}(t)$ be its complement: $S = S(t) + \bar{S}(t)$. Generally $S(t)$ is unknown and is to be determined as part of the solution. The relation between the displacement $u_k(\mathbf{X}, t)$ at any point $(\mathbf{X}, t)$ in the medium and the displacement discontinuity $a_i(\mathbf{X}', t')$ across S was given by equation (3.2.9)*. For a homogeneous, isotropic medium and the case of a planar shear crack, this relation becomes (with slightly different notation for convenience)

$$u_k(\mathbf{X}, t) = \int_0^t dt' \int_{S(t')} K_{\alpha 3 k}(\mathbf{X} - \mathbf{X}', t - t')\, a_\alpha(\mathbf{X}', t')\, dS \qquad (5.1.1)$$

* of K + D
eqn (3.2) of A+R.

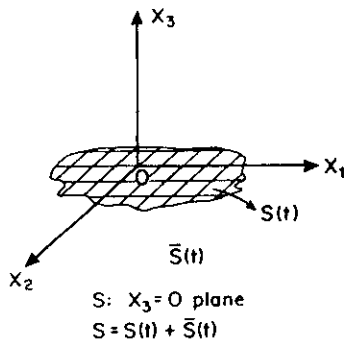

5.1 The geometry of the problem. $S(t)$ is the cracked portion of the $X_3 = 0$ plane.

where Latin subscripts take values 1, 2, 3 and Greek ones the values 1, 2. $K_{\alpha 3k}$ is given by

$$K_{\alpha 3k}(\mathbf{X}, t) = -\mu\left(\frac{\partial U_{k3}}{\partial X_\alpha} + \frac{\partial U_{\alpha k}}{\partial X_3}\right) \tag{5.1.2}$$

where the Einstein summation convention is assumed and U_{ik} is given by (3.3.1). Equation (5.1.1) gives the representation relation throughout the medium. To express the traction perturbation on the fault plane in terms of the slip on it, we evaluate the traction perturbation components $\tau_{\alpha 3}$ by differentiating (5.1.1) and taking the limit as $X_3 \to 0$ to obtain

$$\tau_{\alpha 3}(\mathbf{X}, t) = \int_0^t dt' \int_{S(t')} T_{\alpha\beta}(\mathbf{X} - \mathbf{X}', t - t')\, a_\beta(\mathbf{X}', t')\, dS \tag{5.1.3}$$

where $\mathbf{X}$ and $\mathbf{X}'$ are now the two-dimensional vectors on the fault plane S. The kernel $T_{\alpha\beta}$, obtained by differentiating $K_{\alpha 3k}$, is given by

$$T_{\alpha\beta} = -\mu\left(\frac{\partial^2 U_{33}}{\partial X_\beta\, \partial X_\alpha} + \frac{\partial^2 U_{\beta 3}}{\partial X_3\, \partial X_\alpha} + \frac{\partial^2 U_{\alpha 3}}{\partial X_\beta\, \partial X_3} + \frac{\partial^2 U_{\beta\alpha}}{\partial^2 X_3}\right) \tag{5.1.4}$$

Kernel $T_{\alpha\beta}$ has strong singularities, so the integral in (5.1.3) must be considered to be a principal value. Hence, the solution of (5.1.3) is unique only under additional conditions. Usually, it is sufficient to assume that the slip a_α is smooth everywhere except at the crack edge, where it must be finite. This implies the square-root behavior of the slip a_α near the crack edge (see Section 2.3).

An alternative representation relation is obtained by exploiting the symmetries in the problem. For planar shear cracks, the solution can be shown to be antisymmetric in X_3. That is, the displacement components

u_α and traction perturbation τ_{33} are odd in X_3, whereas u_3 and $\tau_{\alpha 3}$ are even in X_3, and it is sufficient to solve the problem for the upper half-space $X_3 \geq 0$. Furthermore, from the continuity of tractions across $X_3 = 0$ [equation (1.3.25)], it follows that $\tau_{33} = 0$ everywhere on $X_3 = 0$. To obtain the required representation relation, let us first reproduce the Green–Volterra formula (3.1.5) after replacing t_1 by t and t by t' for notational convenience. Then we have

$$\int_0^t dt' \int_S (\sigma_{ij} u_i' - \sigma_{ij}' u_i) n_j \, dS + \int_0^t dt' \int_V \rho (f_i u_i' - f_i' u_i) \, dV$$

$$+ \int_V \rho (u_i \dot{u}_i' - \dot{u}_i u_i') \, dV \Big|_{t'=0}^{t'=t} = 0 \tag{5.1.5}$$

Let us choose as u_i' the three solutions corresponding to the three concentrated unit forces f_i' directed along the X_1, X_2, and X_3 axes and given by

$$f_i' = \delta_{ik} \, \delta(\mathbf{X} - \mathbf{X}') \, \delta(t - t') \qquad \text{for} \quad X_3' > 0, \quad X_3 \geq 0 \tag{5.1.6}$$

where δ_{ik} is the Kronecker delta and $\delta(\mathbf{X})$ and $\delta(t)$ represent the Dirac delta function, and with the initial and boundary conditions

$$u_i' = \dot{u}_i' = 0 \qquad \text{for} \quad t \leq t'; \qquad \sigma_{i3}' = 0 \qquad \text{at} \quad X_3 = +0 \tag{5.1.7}$$

Let us denote the solution u_i' by G_{ik}. Then in (5.1.5) the last term vanishes due to initial conditions, and the terms containing f_i and σ_{i3}' vanish due to the absence of body forces f_i and by (5.1.7), respectively. Taking σ_{ij} as the stress perturbation tensor τ_{ij} and evaluating the term with the δ function, we get

$$u_k(\mathbf{X}, t) = \int_0^t dt' \int_S G_{k\alpha}(\mathbf{X} - \mathbf{X}', t - t') \tau_{\alpha 3}(\mathbf{X}', t') \, dS \tag{5.1.8}$$

Letting $X_3 \to 0$ and accounting for the symmetry of the displacement components, we obtain the required alternative representation relation as

$$a_\alpha(\mathbf{X}, t) = 2 \int_0^t dt' \int_S G_{\alpha\beta}(\mathbf{X} - \mathbf{X}', t - t') \tau_{\beta 3}(\mathbf{X}', t') \, dS \tag{5.1.9}$$

where $\mathbf{X}$ and $\mathbf{X}'$ are now two-dimensional vectors on S. The required components of G are the solution to Lamb's problem and can be expressed in terms of elementary functions. The expressions for $G_{\alpha\beta}$ for

the two- and three-dimensional cases are given in Appendix 1. The kernel $G_{\alpha\beta}$ possesses only weak singularities and can be directly discretized for numerical computation, as we shall discuss in Section 5.2.

Thus, we have obtained two representation relations, (5.1.3) and (5.1.9), both of which relate the slip on the crack plane to the traction perturbation on this plane. These relations comprise a set of mutually inverse integral transforms. If either the slip a_α or the traction perturbation $\tau_{\alpha 3}$ were known everywhere on S, the other of these two quantities could be obtained using (5.1.3) or (5.1.9), respectively. But in a dynamically described source (crack) problem, neither one of them is known everywhere on S. The systems (5.1.3) and (5.1.9) thus simply provide relationships between a_α and $\tau_{\alpha 3}$. Some additional relations between a_α and $\tau_{\alpha\beta}$ on the crack plane are needed to provide the required boundary–integral equations. These relations can be obtained from the constitutive relations on S, as we shall discuss in Section 5.2.

Relations (5.1.3) and (5.1.9) are equivalent in that either of them can be used together with the constitutive relations to solve the crack problem. The variables $\mathbf{X}$ and $\mathbf{X}'$ in (5.1.3) are confined to $S(t)$ since a_α vanishes outside the crack. On the other hand, the integration domain in (5.1.9) covers all points influenced by disturbances that propagate with the fastest wave velocity of the problem (e.g., the compressional wave speed of the medium for general three-dimensional problems). Therefore, one of these two relations may be more efficient than the other for a given problem. For problems in which $S(t)$ is much smaller than S, for example, "interior" crack problems, it is more advantageous to use (5.1.3). For some "exterior" crack problems, the region of traction perturbations is limited, and then (5.1.9) is the more efficient relation. Of course, the domains of integration may coincide for some particular situations – for example, for the case of a self-similar crack propagating with the fastest wave speed of the medium. The domains of integration for the two representation relations are shown in Figure 5.2 for two cases of the interior crack problem. The domain of integration for the exterior problem will be discussed in detail in Section 5.6 under "A circular asperity on an infinite fault plane."

The relation (5.1.3) was essentially formulated by Budiansky and Rice (1979). Burridge (1969) used its two-dimensional form, and Burridge and Moon (1981) its three-dimensional scalar form. The two-dimensional form of (5.1.9) was first used by Kostrov (1966) for dynamic elastic problems and by Das (1976, 1980) for general three-dimensional problems.

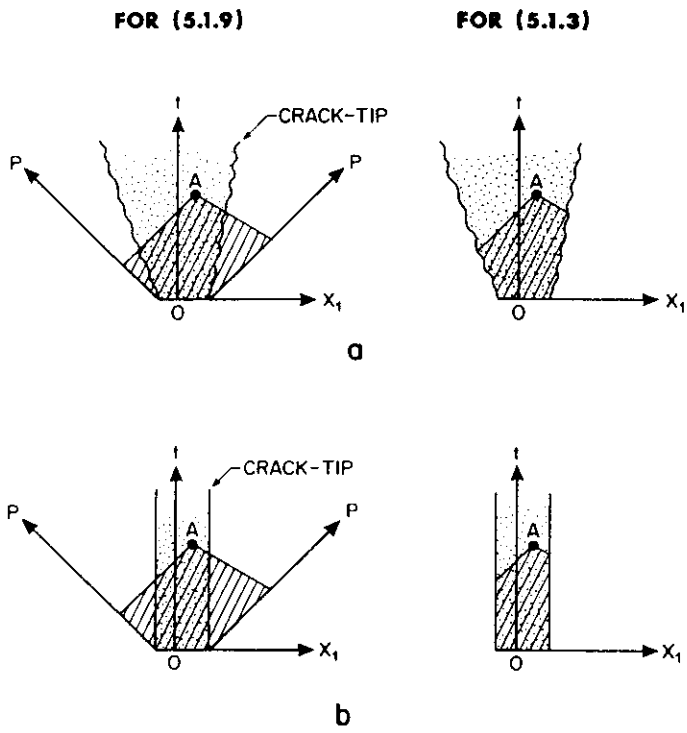

5.2 Cross sections of the domains of integration in the $(X_1 - t)$ plane for the relations (5.1.3) and (5.1.9) for (a) a propagating "interior" crack and (b) a stationary "interior" crack. The crack regions are stippled. The striped areas are the domains of integration for determining the slip at some representative point A, say, within the crack.

In the next section, we discuss the discretization of the representation relations developed here.

5.2 Discrete representations

Let us first discuss the method of discretization of relation (5.1.9). We introduce a regular network of grids centered at the points

$$\begin{aligned} X_1 &= i\,\Delta X, & i &= -\infty, \ldots, -1, 0, 1, \ldots, \infty \\ X_2 &= j\Delta X, & j &= -\infty, \ldots, -1, 0, 1, \ldots, \infty \\ t &= \left(k + \tfrac{1}{2}\right)\Delta t, & k &= 0, 1, \ldots, \infty \end{aligned} \qquad (5.2.1)$$

In each element of the network, we replace the tractions by their average

values over the grid given by (the subscript 3 for the τ_α's being implicit from now on)

$$\tau_{\alpha ijk} = \frac{1}{\Delta t\, \Delta X^2} \times \int_0^{\Delta t} d\tau \iint_{-\Delta X/2}^{\Delta X/2} \tau_\alpha(i\Delta X + \xi_1, j\Delta X + \xi_2, k\Delta t + \tau)\, d\xi_1\, d\xi_2 \tag{5.2.2}$$

We replace the slip a_α by its value at a point within the grid,

$$a_{\alpha ijk} = a_\alpha(i\Delta X, j\Delta X, k\Delta t + \delta t), \qquad 0 \le \delta t \le \Delta t \tag{5.2.3}$$

and we replace the discrete Green function $F_{\alpha\beta}$ by

$$F_{\alpha\beta}(i, j, k) = -2\int_0^{\Delta t} d\tau \int_{-\Delta X/2}^{\Delta X/2} \times G_{\alpha\beta}(i\Delta X + \xi_1, j\Delta x + \xi_2, k\Delta t + \delta t - \tau)\, d\xi_1\, d\xi_2 \tag{5.2.4}$$

Since $G_{\alpha\beta}$ possesses integrable singularities, $F_{\alpha\beta}$ is easily evaluated using (5.2.4). The properties of $F_{\alpha\beta}$ are discussed in detail in Appendix 1. The Green function $F_{\alpha\beta}$ vanishes outside the region $v_P^2 t^2 = X_1^2 + X_2^2$. In particular, if $v_P(\Delta t - \delta t) \le \Delta X/2$, $F_{\alpha\beta}(i, j, 0)$ is nonvanishing only for $i = 0 = j$. This value is

$$F_{\alpha\beta}(0,0,0) = -2\int_0^{\delta t} d\tau \iint_{-\infty}^{\infty} G_{\alpha\beta}(\xi_1, \xi_2, \tau)\, d\xi_1\, d\xi_2 \tag{5.2.5}$$

or, taking into account the homogeneity and symmetry properties of $G_{\alpha\beta}$,

$$F_{\alpha\beta}(0,0,0) = F_0 \delta_{\alpha\beta}\, \delta t \tag{5.2.6}$$

where

$$F_0 = -2\int_0^1 d\tau \iint_{-\infty}^{\infty} G_{11}(\xi_1, \xi_2, \tau)\, d\xi_1\, d\xi_2 \tag{5.2.7}$$

Here F_0 is a positive constant [the minus sign in equations (5.2.4) and (5.2.7) was included to make F_0 positive] independent of the grid size and $\delta_{\alpha\beta}$ is the Kronecker delta. The constant F_0 is the largest element in absolute value of the matrix $F_{\alpha\beta}$. Substituting the discrete forms of τ_α,

a_α, and $G_{\alpha\beta}$ into (5.1.9), we obtain

$$a_{\alpha i j k} = -\sum_{k'=0}^{k}\sum_{i'=-\infty}^{\infty}\sum_{j'=-\infty}^{\infty} F_{\alpha\beta}(i-i', j-j', k-k')\tau_{\beta i' j' k'} + \text{approximation error} \tag{5.2.8}$$

In this expression, with the same order of approximation, the constant F_0 can be replaced by some other positive constant G_0, say, independent of the grid size, which is to be chosen on the basis of stability considerations.

Accordingly, (5.2.8) can be rewritten as

$$a_{\alpha i j k} + \Delta t G_0 \tau_{\alpha i j k} = -\sum_{k'=0}^{k-1}\sum_{i', j' \in S^{\mathrm{P}}_{(k)}} F_{\alpha\beta}(i-i', j-j', k-k')\tau_{\beta i' j' k'} \quad \text{for} \quad i, j \in S^{\mathrm{P}}_{(k)} \tag{5.2.9}$$

where $S^{\mathrm{P}}_{(k)}$ is the union of all grids influenced by disturbances at time $k\,\Delta t$. The stability and approximation error of (5.2.9) are discussed in Appendix 2, where it is shown that

$$0 < \frac{F_0}{G_0} < 2 \tag{5.2.10}$$

is a necessary condition for stability. Relation (5.2.9) is the required discrete form of the representation relation (5.1.9). For a given k, the right side of (5.2.9) depends only on the solution at previous times ($k < k'$) and (5.2.9) is an explicit scheme.

Successful discretization of equation (5.1.3), which would lead to a convenient numerical scheme, has not been achieved. Some possible approaches are discussed by Burridge (1969) and by Burridge and Moon (1981). Instead of discretizing (5.1.3), we shall use the fact that (5.1.3) is an integral transform, inverse to (5.1.9), and construct an inverse of the discrete transform (5.2.8). This inverse transform, like the direct transform (5.2.8), must be a discrete convolution transform; that is, its kernel will depend only on differences:

$$\tau_{\alpha i j k} = -\sum_{k'=0}^{k}\sum_{i'=-\infty}^{\infty}\sum_{j'=-\infty}^{\infty} S_{\alpha\beta}(i-i', j-j', k-k')a_{\beta i' j' k'} \tag{5.2.11}$$

Then, application of transform (5.2.8) to this kernel must give the unit

kernel:

$$\sum_{k'=0}^{k}\sum_{i'=-\infty}^{\infty}\sum_{j'=-\infty}^{\infty} F_{\alpha\beta}(i-i', j-j', k-k') \times S_{\beta\gamma}(i'-i'', j'-j'', k'-k'') = \delta_{\alpha\gamma}\delta_{ii''}\delta_{jj''}\delta_{kk''} \tag{5.2.12}$$

To determine $S_{\alpha\beta}$, we obtain the explicit numerical scheme from (5.2.12):

$$\Delta t G_0 S_{\alpha\gamma}(i, j, k) = -\sum_{k'=0}^{k-1}\sum_{i'=-\infty}^{\infty}\sum_{j'=-\infty}^{\infty} F_{\alpha\beta}(i-i', j-j', k-k') \times S_{\beta\gamma}(i', j', k') + \delta_{\alpha\gamma}\delta_{i0}\delta_{j0}$$

Equation (5.2.11) can be written in a form similar to (5.2.9) as

$$\tau_{\alpha i jk} + S_0 a_{\alpha i jk} = -\sum_{k'=0}^{k-1}\sum_{i', j' \in S_{(k')}} S_{\alpha\beta}(i-i', j-j', k-k') a_{\beta i' j' k'} \quad \text{for} \quad i, j \in S_{(k)} \tag{5.2.13}$$

where $S_{(k)}$ is the union of all grids with nonvanishing slip and the tip element $S_0 = S_{11}(0,0,0) = 1/(\Delta t G_0)$ and is a positive constant. (The sign of F_0, G_0, and S_0 becomes important in problems where friction acts on the fault faces.) Note that using (5.2.9) is exactly equivalent to using (5.2.13) for a particular problem; that is, the solutions using the two algorithms must coincide, apart from different rounding error accumulation. The properties of $S_{\alpha\beta}$ are discussed in Appendix 2.

The approach of discretizing $T_{\alpha\beta}$ by inverting $F_{\alpha\beta}$ has two advantages. First, one can use the simple discrete representations of τ_α and a_α, that is, (5.2.2) and (5.2.3), which can be shown to be good approximations by comparing the results with analytical solutions of simple problems (an example of which is given in the next section). Direct discretization of $T_{\alpha\beta}$ may require some different representation for τ_α and a_α. Second, and more important from the practical point of view, $F_{\alpha\beta}$ is a well-behaved matrix and can be inverted without reservation. Furthermore, since $F_{\alpha\beta}$ is quite sparse, one does not actually have to invert a very large matrix [$F_{\alpha\beta}$ will consist of $(N^2T)^2$ elements if N^2 is the number of perturbed spatial grids on the fault plane and T the maximum time level for which $S_{\alpha\beta}$ is desired] but may determine $S_{\alpha\beta}$ by an explicit time-stepping procedure.

It was mentioned in Section 5.1 that representation (5.2.13) is more economical than representation (5.2.9) for "interior" crack problems,

whereas the situation is reversed for "exterior" crack problems. Let us quantify this efficiency for the numerical solution of a stationary crack – that is, a finite crack that slips without growing. In general, in seismology one is interested only in the slip distribution on the crack, because it completely determines the radiation from the crack through the asymptotic form of (5.1.3), that is, equation (3.2.11). The traction distribution outside the crack, in this context, is of interest at most in the vicinity of the crack edge. The number of grid values that are relevant at a fixed time step is proportional to the crack area in this case, whereas the number of traction values involved in algorithm (5.2.9) is proportional to the square of time. The number of arithmetic operations necessary to obtain the solution at the kth time step is proportional to k^6, and the necessary storage is proportional to k^3, when using (5.2.9). So every doubling of the number of time steps requires eight times more storage and sixty-four times longer computation time. For the stationary crack problem under discussion here, the number of slip values is proportional to k and the number of arithmetic operations when using (5.2.13) is proportional to k^2, and the storage required is proportional to k. Thus, for this problem, using (5.2.13) would be k^4 times faster and require k^2 less storage. Since the two algorithms are equally efficient for a self-similar crack propagating at the fastest wave speed of the medium, the economy in using (5.2.13) over (5.2.9) for interior problems increases with slower and slower crack speeds. Similar comparisons of efficiency can be made for exterior problems, with the above considerations applying in reverse. Algorithm (5.2.9) was first used by Hamano (1974) for two-dimensional crack problems and by Das (1980) for three-dimensional problems.

We shall now proceed to apply the algorithms developed here to some specific dynamic crack problems. In general, we shall consider only three-dimensional cases except when appropriate solutions do not exist, in which case a two-dimensional illustration will be used.

5.3 The circular self-similar shear crack

We consider the three-dimensional problem of a self-similar circular shear crack, which is initiated at a point and propagates at a known constant velocity, v say. The assumption of a constant fracture speed is rather unphysical, because it violates principles of fracture mechanics. A stress singularity that grows in time, as the stress singularity at the growing crack edge does, is unlikely to result in a constant fracture speed under any of the fracture criteria discussed in Chapter 2,

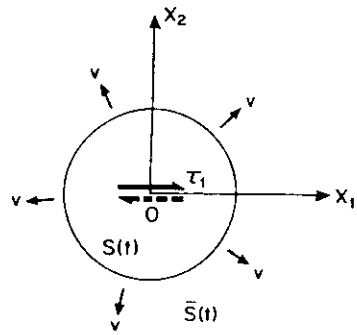

5.3 Geometry of the self-similar circular shear crack.

unless the fracture toughness distribution on the fault plane is rather pathological. Spontaneous crack problems are more physical, and we shall devote a large part of this chapter to them. It is instructive, however, to discuss the self-similar problem since it is the simplest possible case and is useful for demonstrating the numerical method, including its accuracy and stability. Historically, more than two decades ago, this problem was the first dynamic three-dimensional shear problem to be solved.

The crack region $S(t)$ is known and given by

$$S(t): X_1^2 + X_2^2 \leq v^2 t^2$$

The geometry of the problem is shown in Figure 5.3. We shall solve the problem when the stress drop on $S(t)$ is prescribed to be a constant, $\Delta\sigma$, say.[1] Without loss of generality for the circular crack problem, we may assume that the stress drop is directed in the X_1 direction. Then we have the mixed boundary value problem

$$\tau_1 = \Delta\sigma, \tau_2 = 0 \quad \text{on} \quad S(t); \qquad a_\alpha = 0 \qquad \text{on} \quad \bar{S}(t)$$

After discretization, we obtain

$$\tau_{1ijk} = \Delta\sigma, \tau_{2ijk} = 0$$

$$\text{for} \quad S_{(k)}: (i\Delta X)^2 + (j\Delta X)^2 \leq v^2\left(\frac{k+1}{2}\right)^2(\Delta t)^2 \quad (5.3.1)$$

$$a_{\alpha ijk} = 0 \quad \text{for} \quad \bar{S}_{(k)}: (i\Delta X)^2 + (j\Delta X)^2 > v^2\left(\frac{k+1}{2}\right)^2(\Delta t)^2$$

[1] The term "stress drop" has traditionally been used in seismology to mean traction drop, and we shall continue to use the term in this sense.

Taken together with (5.2.9) or (5.2.13) this gives the complete formulation of the problem.

We first use (5.2.9) to solve the problem. We denote its right side by, say, $L_{\alpha i j(k-1)}$, that is,

$$L_{\alpha i j(k-1)} = -\sum_{k'=0}^{k-1} \sum_{i', j' \in S^{P}_{(k')}} F_{\alpha\beta}(i-i', j-j', k-k')\tau_{\beta i' j' k'}$$

$$\text{for} \quad i, j \in S^{P}_{(k)}$$

where $S^{P}_{(k)}$ was defined in the last section. The term $L_{\alpha i j(k-1)}$ depends on the values of τ_α at all previous time steps and is thus known at any time step if the traction history up to the previous time step is known. The summation in $L_{\alpha i j(k-1)}$ extends over the entire cone of dependence of the grid point $(i\Delta X, j\Delta X, (k+\frac{1}{2})\Delta t)$ except the grid point itself. Then we can rewrite (5.2.9) as

$$a_{\alpha i j k} + \Delta t G_0 \tau_{\alpha i j k} = L_{\alpha i j(k-1)}$$

It follows very simply from this that, under the mixed boundary conditions (5.3.1), the solution is given by

$$\begin{aligned} a_{\alpha i j k} &= -\delta_{\alpha 1}\Delta t G_0 \Delta\sigma + L_{\alpha i j(k-1)} \\ \tau_{\alpha i j k} &= \delta_{\alpha 1}\Delta\sigma \qquad \text{on} \quad S_{(k)} \end{aligned} \tag{5.3.2}$$

and by

$$\tau_{\alpha i j k} = \frac{L_{\alpha i j(k-1)}}{\Delta t G_0}; \qquad a_{\alpha i j k} = 0 \qquad \text{on} \quad \bar{S}_{(k)} \tag{5.3.3}$$

where $\delta_{\alpha 1}$ is the Kronecker delta. Since the initial $L_{\alpha i j(k-1)}$ is zero by definition, this is an explicit scheme to determine slip and traction perturbation everywhere on the crack plane.

Let us now solve the same problem using the discrete representation (5.2.13). We denote its right side by, say, $M_{\alpha i j(k-1)}$, that is,

$$M_{\alpha i j(k-1)} = -\sum_{k'=0}^{k-1} \sum_{i', j' \in S_{(k')}} S_{\alpha\beta}(i-i', j-j', k-k')a_{\beta i' j' k'}$$

$$\text{for} \quad i, j \in S_{(k)}$$

where $S_{(k)}$ was defined earlier. The term $M_{\alpha i j(k-1)}$ depends on the values of a_α at all previous time steps and is thus known at any time step if the slip history up to the previous time step is known. The summation in $M_{\alpha i j(k-1)}$ extends over the intersection of the cone of dependence of the point $(i\Delta X, k\Delta X, (k+\frac{1}{2})\Delta t)$ with the crack area $S_{(k)}$ but excluding

this point itself, that is, over a smaller region than when (5.2.9) was used. We can now rewrite (5.2.13) as

$$\tau_{\alpha i jk} + S_0 a_{\alpha i jk} = M_{\alpha i j(k-1)}$$

The solution to this under the mixed boundary conditions (5.3.1) is very simply

$$\tau_{\alpha i jk} = \delta_{\alpha 1}\,\Delta\sigma; \qquad a_{\alpha i jk} = -\frac{\delta_{\alpha 1}\,\Delta\sigma + M_{\alpha i j(k-1)}}{S_0} \qquad \text{on} \quad S_{(k)} \tag{5.3.4}$$

This is an explicit scheme for finding $a_{\alpha i jk}$ on $S_{(k)}$ since $M_{\alpha i j(k-1)}$ is known to be zero initially and gives the required slip on the crack. If the solution for the stress $\tau_{\alpha i jk}$ on $\bar{S}(k)$ is desired, it can be easily obtained as

$$a_{\alpha i jk} = 0; \qquad \tau_{\alpha i jk} = M_{\alpha i j(k-1)} \tag{5.3.5}$$

It is important to note that the solutions for the traction perturbation and slip are homogeneous functions of zeroth order of the coordinates and time for self-similar problems (definition of self-similarity).

We shall now compare the numerical solution using the two forms of the representation relations with the corresponding analytic self-similar solution. Let us consider the case in which the fracture velocity $v = v_P/2$. The results are shown in Figure 5.4 for the case of a Poisson solid. (In the remainder of the book all numerical results will be illustrated for the Poisson solid only.) The required analytic solution for the slip a_α is obtained by integrating equation (3.4.18) with respect to time and substituting $v = v_P/2$. The numerical solutions are determined from (5.3.2), (5.3.3) and from (5.3.4), (5.3.5) for the two forms of the representation relations. The two numerical methods yield solutions that are identical except at the last decimal place, as expected. Since the initial crack in a numerical method cannot be infinitesimal, one cannot in fact numerically study a self-similar crack. In this example, an initial crack of radius ΔX is assumed to appear instantaneously and start extending at a speed of $v_P/2$. In other words, the analytic and numerical solutions are really solutions of different problems. However, at larger and larger times, the effect of this initial difference is expected to become less and less significant. The normalized half-slip U is plotted in units of $(20\,\Delta\sigma\,\Delta X)/3\mu$ and the normalized time T is plotted in units of $v_P/\Delta X$. The analytic solution for the half-slip is shown by the continuous line in Figure 5.4; its numerically calculated values are shown by crosses at

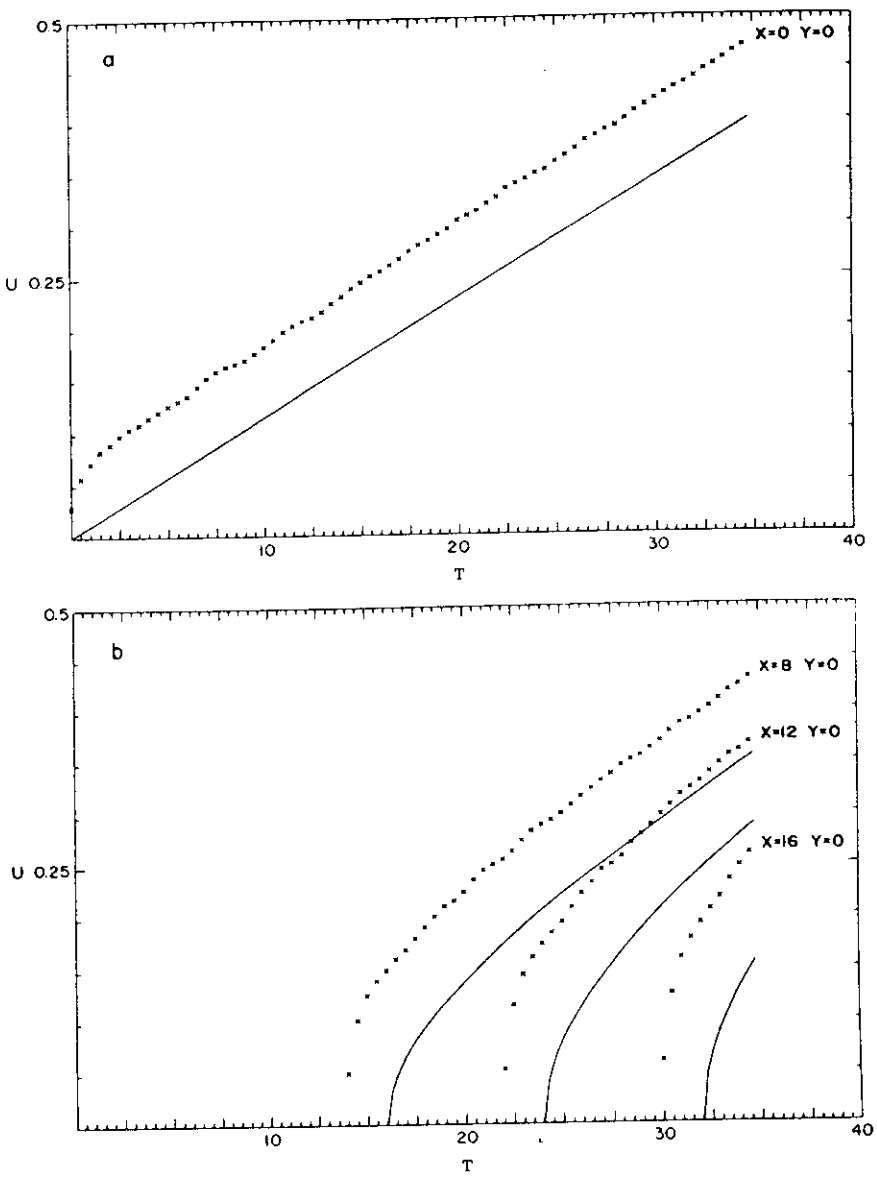

5.4 Normalized half-slip U versus normalized time T for a circular crack propagating at a speed $v_p/2$. The analytic solution is indicated by solid lines, and the numerical solution for the instantaneously appearing circular crack of radius ΔX is indicated by crosses. $X = X_1/\Delta X$; $Y = X_2/\Delta X$. The solution is plotted at points (a) and (b) along the X_1 axis, (c) along the X_2 axis, (d) along a line at 45° to the axes [the analytic solution is omitted to increase clarity in (d)]. The spatial to temporal grid size ratio is given by $v_p\,\Delta t/\Delta X = .5$.

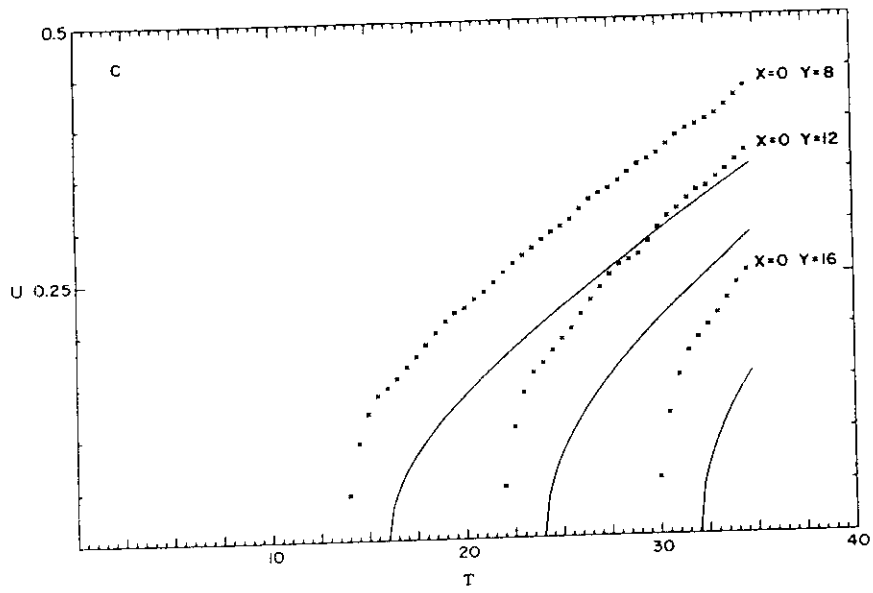
c
0.5
U 0.25
X=0 Y=8
X=0 Y=12
X=0 Y=16
10
20
30
40
T

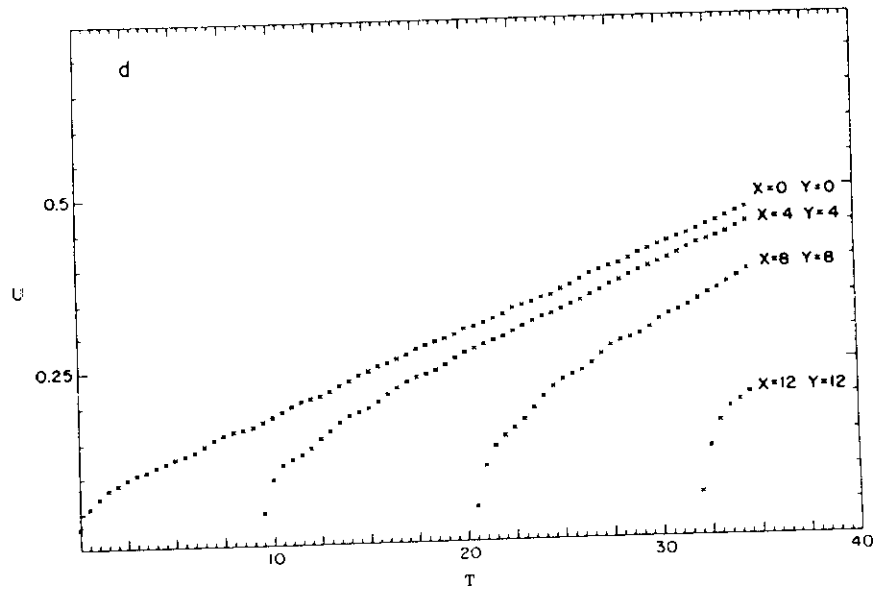
d
0.5
U
0.25
X=0 Y=0
X=4 Y=4
X=8 Y=8
X=12 Y=12
10
20
30
40
T

5.4 (*cont.*)

points along the X_1 and X_2 axes and along a line at 45° to the two axes. The numerical solution always lies above, that is, is larger than the analytic solution owing to the above-mentioned initial difference. What is most important, however, is that the *rate* of increase of slip with time is the same for the analytic and numerical solutions except for the first few time steps of the solution. To ensure stability, G_0 was taken as $2F_0$, which satisfies the necessary criterion for stability given by (5.2.10). We note that the square-root form of the slip a_1 is well approximated numerically. The slip component a_2 on the crack was always found to be less than 3 percent of a_1; in other words, it is practically negligible (it is identically zero in the analytic case). In fact, the maximum values of a_2 are concentrated in grids near the crack edge, which in a numerical scheme is necessarily smeared out, and in the interior of the crack its values are even smaller. The values of a_2 can be considered a measure of the numerical noise in the solution. Thus, the slip is in the direction of the stress drop on the fault plane for the circular self-similar crack. Figure 5.4 also shows that the numerically determined slip is azimuthally symmetric (as the analytic one is) without the *a priori* imposition of such a condition. The three-dimensional self-similar circular shear crack problem was numerically studied by Madariaga (1976), Archuleta (1976), and Das (1980), among others.

So we have used the numerical boundary–integral method in its two forms to study a simple self-similar problem and showed that the results compare well with its analytic solution for one particular fracture speed. In a similar way, any crack problem with given stress drop on the fault plane and crack speed (neither of these need be constant and the speed need not be the same in all directions) can be solved following the above development. It includes as a special case the stationary crack problem studied by Madariaga (1976) and by Das (1980).

5.4 The finite circular shear crack

Next we consider the problem of a circular shear crack that initiates at a point, propagates at a preassigned constant velocity v, say, and stops when it reaches some finite radius r, say. Let the stress drop on the crack be assigned a constant, $\Delta\sigma$, say, and directed in the X_1 direction. The crack region $S(t)$ is defined by

$$\begin{aligned} S(t): X_1^2 + X_2^2 &\le v^2t^2 \quad \text{for} \quad vt \le r; \\ X_1^2 + X_2^2 &= r^2 \quad \text{for} \quad vt > r \end{aligned} \tag{5.4.1}$$

//

Then we have the mixed boundary value problem

$$\tau_1 = \Delta\sigma, \tau_2 = 0 \quad \text{on} \quad S(t); \qquad a_\alpha = 0 \quad \text{on} \quad \bar{S}(t) \tag{5.4.2}$$

This problem can be solved numerically following the procedure outlined in detail in the last section, the discrete crack area $S_{(k)}$ now being defined as

$$S_{(k)}: \begin{cases} (i\Delta X)^2 + (j\Delta X)^2 \le v^2\left(k + \tfrac{1}{2}\right)^2(\Delta t)^2 \\ \qquad\qquad\qquad\qquad \text{for} \quad v\left(k + \tfrac{1}{2}\right)\Delta t \le r \\ (i\Delta X)^2 + (j\Delta X)^2 = r^2 \qquad \text{for} \quad v\left(k + \tfrac{1}{2}\right)\Delta t > r \end{cases}$$

Even this relatively simple problem of a finite dynamic crack cannot be solved analytically, though a kinematic description using the results of the self-similar problem was considered by Sato and Hirasawa (1973).

Let us apply the numerical algorithm (5.2.13) to this problem. We consider an instantaneously appearing crack of diameter $3\Delta X$, which grows to a final diameter of $41\,\Delta X$ at a speed $v = v_P/2$. We shall allow backslip to occur on the crack in this example. The half-slip $a_1/2$ is plotted against time in Figure 5.5 and is normalized by $(r\Delta\sigma)/3\mu$ for this problem. The slip on the crack is found to be essentially in the direction of the stress drop even after the crack has stopped, and it coincides with the solution of the corresponding self-similar problem until the first diffracted waves from the crack edge arrive and decrease the slip rate. The rise time and slip at the center are larger than at the crack edge. The dynamic slip is found to overshoot the static value, but when backslip is allowed on the crack, as it is here, it decreases from its maximum value and approaches the static value.

From some simple geometric considerations, it is possible to obtain a rough estimate of the dynamic overshoot expected at a point within the crack. A point on the crack continues slipping until some (diffracted) wave from the crack edge returns to it. Let this wave have velocity v_H. Then the displacement expected at a point on the crack is given by the solution of the dynamic self-similar circular crack propagating at the speed v. The overshoot OV on the crack varies with position on the crack, being largest at the center and smallest at the edge. At the center, the overshoot is given by

$$OV \approx \frac{A(v)}{A(0)}\left(1 + \frac{v}{v_H}\right) - 1$$

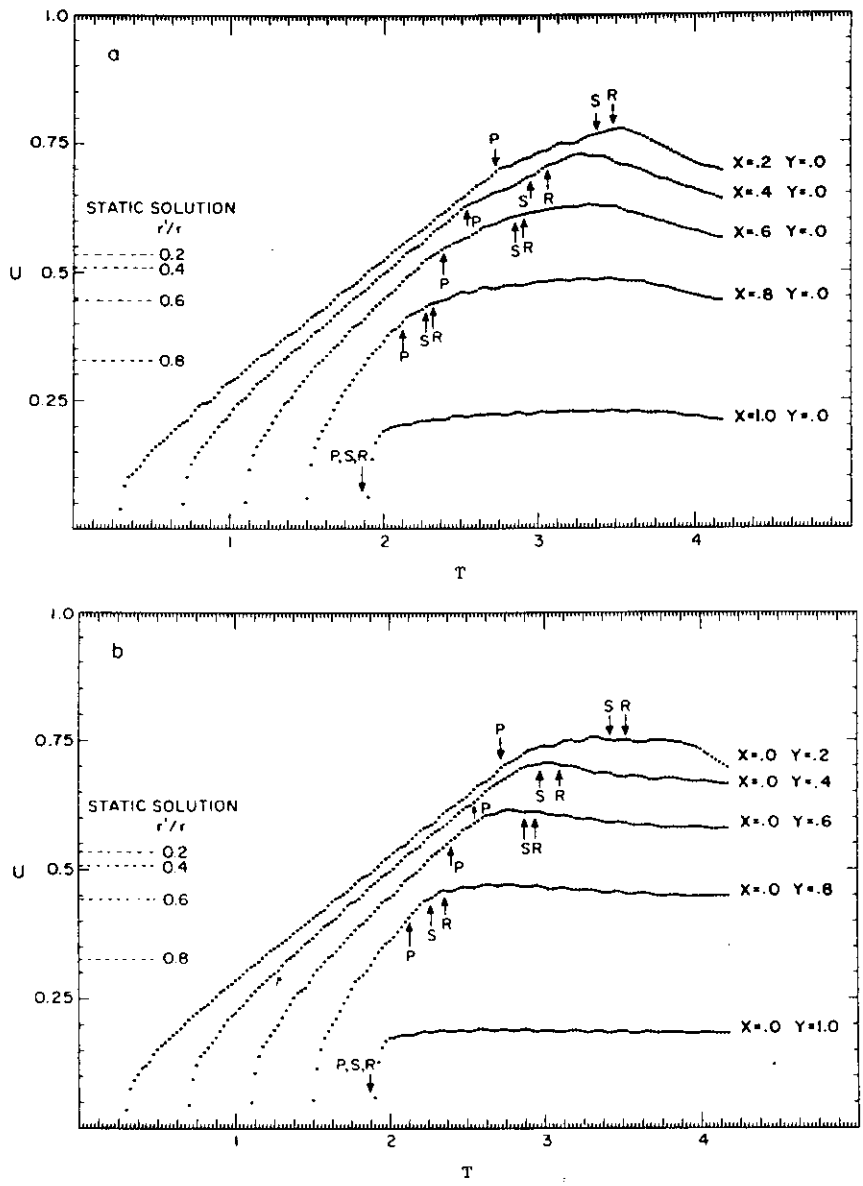

5.5 Normalized half-slip U versus normalized time $T = v_P' t/r$ for a finite circular crack for (a) points along the X_1 axis and (b) points along the X_2 axis. $X = X_1/r$, $Y = X_2/r$, r being the final crack radius, and $v_P \Delta t/\Delta X = .5$. The theoretical arrival times of the diffracted P, S, and Rayleigh waves from the crack edge are indicated on each curve by arrows. The static solutions for the points $r'/r = .2, .4, .6$, and $.8$, where r' is the distance of the point from the center of the crack, are given by $U = .55\sqrt{1 - r'^2/r^2}$ and marked along the abscissas.

where $A(v)/A(0)$ was plotted in Figure 3.6 as a function of v. For $v = v_P/2$, this overshoot is $0.85(1 + v_P/2v_H) - 1$. A lower bound of this overshoot would be obtained for $v_H = v_P$, that is, if the wave that stops the slip is the P wave. This lower bound at the center of the crack is ~ 28 percent above the corresponding static slip from the above formula. Figure 5.5 shows that the maximum slip is reached at or soon after the time when the Rayleigh wave arrives from the crack edge. Then, taking $v_H = v_R$, the Rayleigh wave velocity, one obtains a very rough estimate of the upper bound of the overshoot at the crack center as ~ 65 percent. This is a very rough estimate since it assumes that the P and/or S waves from the crack edge did not modify the slip determined by the dynamic self-similar solution (an assumption that is seen from Figure 5.5 to be not quite valid!). At the crack edge the overshoot is

$$OV \approx \frac{A(v)}{A(0)}\sqrt{1 + v/v_H} - 1$$

so that for $v_H = v_P$, the edge overshoot is ~ 4 percent, and for $v_H = v_R$, it is ~ 18 percent of its static value. The static values of U are shown in Figure 5.5, and the central overshoot in the numerical case was found to be ~ 36 percent. Estimates of this overshoot, obtained by Madariaga (1976), Archuleta (1976), Das (1980), and others using different numerical methods and/or different grid sizes and without allowing backslip were found to lie between 20 and 27 percent. The dynamic overshoot of slip in the interior of the crack may, of course, be interpreted as the overshoot of the static stress drop there. The above formulas also show that the dynamic overshoot increases with increasing crack speed v. Obviously for a given problem (solved by the same method and using the same discretization of the problem), the overshoot must be greater when backslip is disallowed on the fault. Hence, in obtaining an estimate of the static solution, allowing backslip would give a better estimate than disallowing it.

ANALYITICAL SOLUTION FOR SLIP RATE ON A SELF-SIMILAR PROPAGATING CRACK, RUPTURE VELOCITY BEING LESS THAN THE RAYLEIGH WAVE SPEED (OR EQUAL TO) OF THE ELASTIC MEDIUM.

CIRCULAR CASE

For a self-similar, circular shear crack with constant stress drop $\Delta\sigma$, the slip rate distribution is (Kostrov, 1964)

$$\dot{a} = \frac{tA}{\left(t^2 - x_i x_i / v^2\right)^{1/2}} \qquad \text{for} \quad x_i x_i < t^2 v^2 \tag{3.4.18}$$

Here, v is the constant fracture velocity, which is $\leq v_R$, the Rayleigh wave velocity, and A is given by

$$A = \frac{4\,\Delta\sigma}{\mu I(v)} \tag{3.4.19}$$

where $I(v)$ is a smooth function of v given by

$$I(v) = \left(\frac{v^2}{v_S^3}\right)\int_0^\infty \left\{(2\nu + 1)^2 - 4\nu\left(\gamma^2 + \nu\right)^{1/2}(1 + \nu)^{1/2} + 1 + \nu\right\} \times \frac{d\nu}{\left[1 + \nu\left(v^2/v_S^2\right)\right]^2 (1 + \nu)^{1/2}} \tag{3.4.20}$$

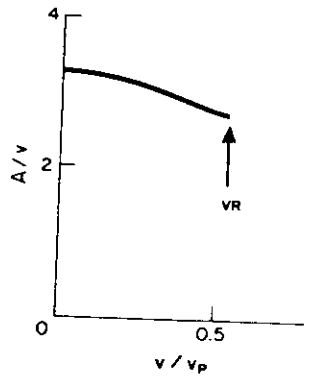

3.6 A/v, normalized by its static value, versus fracture speed v.

and $\gamma = v_S/v_P$.[1] Here A/v gives the ratio of slip versus crack radius and is plotted against v in Figure 3.6, its value being normalized by the static value $24\,\Delta\sigma/7\pi\mu$.

[1] Performing the integration in (3.4.20), we can write $I(v)$ in closed form as

$$I(v) = \alpha^4\left\{12(\gamma - 1) - \frac{12\alpha^4 - 21\alpha^2 + 8}{(\alpha^2 - 1)^{(3/2)}}\tan^{-1}\sqrt{\alpha^2 - 1} + \frac{12\alpha^2 - 8\gamma^2}{\sqrt{\alpha^2 - \gamma^2}}\tan^{-1}\frac{\sqrt{\alpha^2 - \gamma^2}}{\gamma} + \frac{\alpha^2 - 2}{\alpha^2(\alpha^2 - 1)}\right\} \tag{3.4.20a}$$

where $\alpha^2 = v_S^2/v^2$.

ELLIPTICAL CRACK

Burridge and Willis (1969) solved a more general problem, in which the fracture velocity depended on the direction, so that the crack at all times had an elliptical shape, given by

$$\frac{x_1^2}{v_1^2} + \frac{x_2^2}{v_2^2} \leq t^2 \tag{3.4.24}$$

where v_1 and v_2 are the fracture speeds in the x_1 and x_2 directions, respectively. It was found that the slip direction coincides with the direction of stress drop, when it is parallel to one of the axes of the ellipse. The distribution of slip rate magnitude is

$$\dot{d}(\mathbf{x}, t) = \frac{At}{\left(t^2 - x_1^2/v_1^2 - x_2^2/v_2^2\right)^{1/2}} \tag{3.4.25}$$

where A is proportional to the stress drop $\Delta\sigma$. The expression for A has the form of a complicated surface integral, which depends on the velocities v_1 and v_2.

Far-field radiation

For "crack" problems.

It can be proved that the far-field P and S wave pulse shapes $S(t)$ are given by the sum of the slip rate on the fault at a given time t i.e.

$$S(t) = \frac{d}{dt} \sum a(t)$$

where $S(t)$ is the pulse shape, and the summation (integral for the continuous problem) extends over the broken area of the fault.

For "asperity" problems, it is the sum of the stress changes over the area occupied by the initial asperity

$$S(t) = \frac{d}{dt} \sum \tau(t)$$

6.3 The heterogeneous faulting process

We saw in the last chapter that the fracture process depends on the initial stress distribution on the fault and on the physical properties of the fault such as its strength and its static and dynamic friction levels. Variations in any one of these parameters over the crack plane would produce variations in the fracture velocity, slip rate, and stress drop distribution over the fault. This heterogeneity would be manifested in the complexity of the radiated pulse shapes. Such observations of "multiple shocks" led to the introduction and subsequent acceptance of models with heterogeneous stress drop and strength over the fault plane. Two idealizations of this situation have been considered in the past decade. In one, known as the "barrier" model, the stress drop on the fractured part of the fault plane is essentially uniform and the critical stress level has large variations. In the other, known as the "asperity" model, the stress drop is highly variable over the fault. Obviously, every conceivable variation and combination of these two extreme cases is plausible in reality. Also, instead of one unique crack edge, there may be multiple crack edges due to the locking of regions behind the main crack edge. The stress drop in this case becomes inhomogeneous not only in space but in time as well. A problem of random variation of stress drop and strength over the fault was studied numerically by Mikumo and Miyatake (1979), though with a somewhat simplified model. The fracture process was found to be quite chaotic, with no clearly distinguishable fracture front. In such cases, a stochastic or a fractal approach may be instrumental.

It is now well known that some aftershocks occur off the main fault plane. Obviously, a complex seismic event may be accompanied by such shocks, occurring during the main earthquake rather than after it. This implies that at least part of the complexity of seismic radiation cannot be assigned to the main fault plane as is assumed in the models mentioned here. This is especially true when one is considering the high-frequency radiation from an earthquake.

In this section, we shall consider only some simple examples of these variations confined to the fault plane and determine the far-field seismic radiation due to fracture propagation on such a plane.

The barrier model

A barrier may be characterized by some measure of its areal extent and some measure of its strength. We may use the parameter S, defined in Section 5.6, to denote the relative strength of the barrier. If the areal extent of the barrier is large, the crack edge propagation will be arrested. But if its areal extent is small compared with the instantaneous crack dimension at the time it is encountered by the crack edge, the crack edge and the barrier will interact in the three different ways, depending on the value of S:

1. If S is small, the barrier will be broken as the crack edge encounters it.

2. If S is very large, the crack edge will propagate around it, leaving behind an unbroken region.
3. If S has some intermediate value, the barrier will not be broken the first time it is encountered by the crack front but will eventually break due to the subsequent concentration of stress on it during the dynamic growth and slip of the surrounding areas.

The presence of such barriers on the fault will introduce diverse slip functions over the fault, which in turn will be seen as complexity in the radiated seismic wave forms and will modify the seismic moment of the earthquake. This problem was first studied two dimensionally by Das and Aki (1977b) and by Das (1985) for the three-dimensional case. Since the two-dimensional results are very complete and are now well known, we shall include only these results here. The three-dimensional calculations show that the two-dimensional results correctly predict the complexity of the far-field waveforms for a fault with barriers.

Let us confine our discussion to the unilateral propagation of an inplane crack. The four cases studied are listed below. The total crack length is taken as $10\,\Delta X$ and $S = 0$ in the areas without barriers for all the cases. The latter parameter value means that a critical crack length of zero is needed for dynamic propagation, which makes the calculations very economical. Backslip will not be allowed in all cases so that $a_{\alpha i j k_2'} > a_{\alpha i j k_1'}$, where $k_2' > k_1'$. Hence $A^{\mathrm{P}}_{\mathrm{initial}}(k\,\Delta t, \mathbf{m})$ is positive for all time and the maximum value of the amplitude spectrum is at zero frequency.

Case P-SV-0: There are no barriers on the fault, this case being included purely for the purpose of comparison. The crack extends at a speed close to v_{P} due to S being chosen as zero. The distribution of S and the resulting slip on the fault are shown in Figure 6.3. The far-field P pulse shape determined from equation (6.1.4) and the corresponding amplitude spectra are given in Figure 6.4.

Case P-SV-1: One strong barrier exists on the fault, and it remains unbroken when the dynamic fracture process on the fault is completed. The distribution of S and the slip on the fault are shown in Figure 6.5, and the far-field radiated field is plotted in Figure 6.6. The spectra for the case P-SV-0 is indicated in the latter figure by dashed lines.

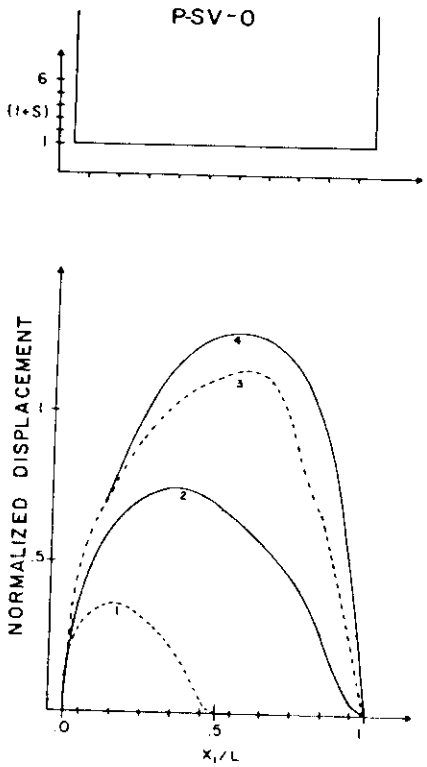

6.3 Distribution of the parameter S and "snapshots" of the distribution of the normalized half-slip $a_1/2$ over the fault length for case P-SV-0. The half-slip is normalized by $L\Delta\sigma/3\mu$, where L is the fault length and the integer next to each curve indicates the time measured in units of $.5L/v_P$. (*From Das and Aki, 1977b. © Am. Geophys. Union.*)

Case P-SV-2: Two unbreakable barriers exist on the fault. Figure 6.7 and Figure 6.8 show the corresponding S, the slip on the fault, and the far-field radiation. The dashed lines again give the P-SV-0 spectra.

Case P-SV-3: The two barriers on the fault, having intermediate S values, do not break at the initial passage of the fracture front but break before the completion of the dynamic fracture and slipping process is completed. The related parameters and results are shown in Figures 6.9 and 6.10.

The major conclusions drawn from this example can be summarized as follows:

1. The smooth fault P-SV-0 and the P-SV-3 fault result in single earthquakes, whereas the heterogeneous faults P-SV-1 and P-SV-2 result in multiple shocks.
2. The time history of slip on the fault and the resulting far-field radiation are most complicated in the case when the initially unbreakable barrier eventually breaks (P-SV-3). In this case the duration of the fracture and slipping process are longer than in the other cases for the same fault length.
3. The final slip on the fault and hence the seismic moment are largest for the smooth crack (P-SV-0) and smallest for the case of the fault with two unbroken barriers (P-SV-2). In the case of the barrier that eventually breaks, the final slip and moment are almost as large as those for the smooth fault. The slip for the fault with two unbreakable barriers has the most uniform value over the fault, whereas the fault with no barriers at the end of the fracture process (P-SV-0 and P-SV-3) shows the largest amount of variation in slip distribution over the fault! This may explain why the uniform dislocation model (Haskell, 1964) has often been able to explain observed overall features of seismograms satisfactorily.
4. Clear directivity effects in the seismic radiation are seen in all cases, these effects being stronger for the fault with unbreakable barriers than for the smooth fault. However, when the barriers eventually break the directivity effect is even weaker than that for the smooth fault.
5. The time domain pulses are more sensitive to the complexity of the fracture process than the spectral shapes. In particular, when the barriers eventually break the pulses show complexity in all directions from the source, but the spectra are not particularly revealing.
6. When the barriers remain unbroken, the spectra at the highest frequencies for which the numerical results are meaningful (this

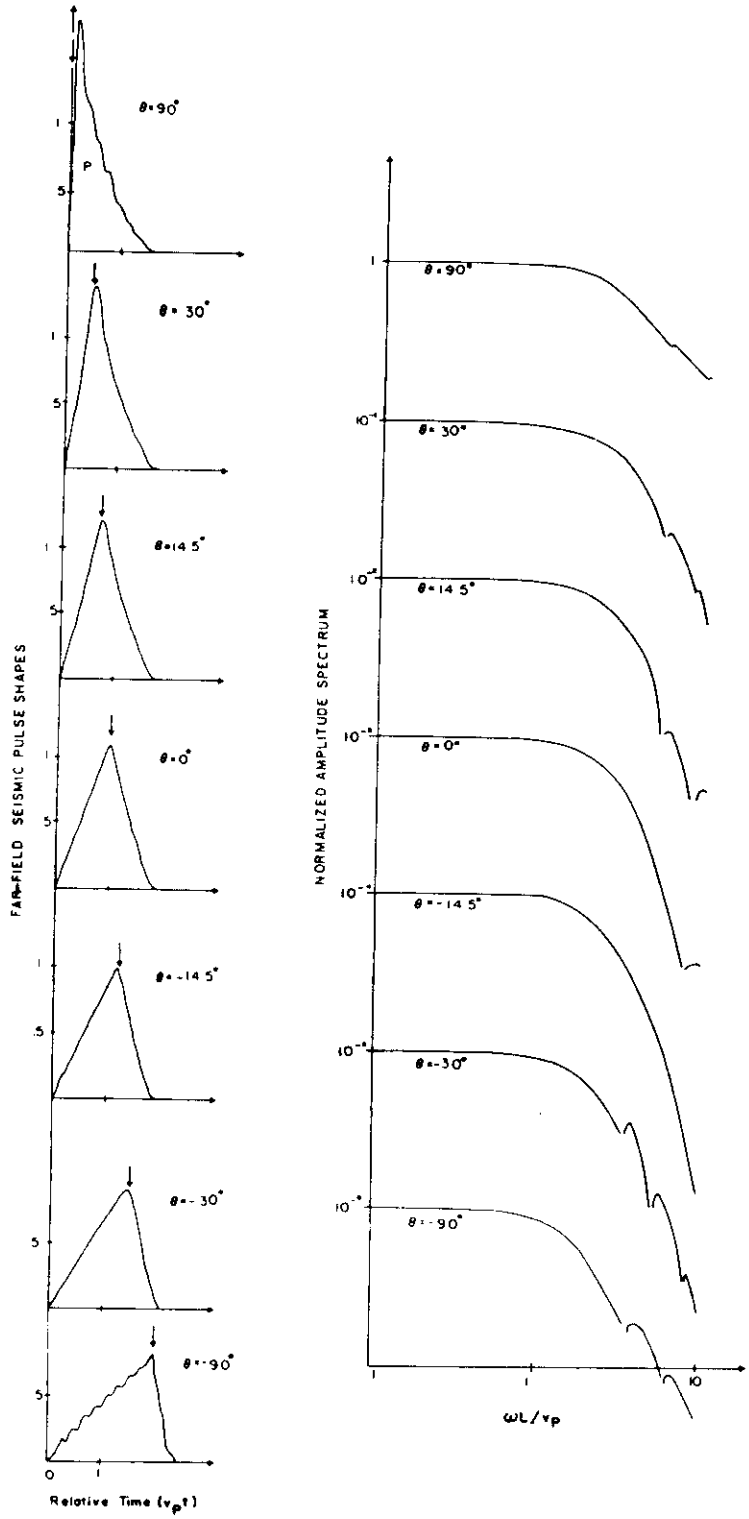

6.4 Far-field P-wave displacement pulse shape and amplitude spectra for various directions from the fault for case P-SV-0. The angle θ is measured from the normal to the fault. The arrows indicate the arrival of the first diffracted wave when the crack tip stops. For $\theta = 0°$ the P- and S-wave pulse shapes coincide. The amplitude spectra are normalized by their value at zero frequency. (*From Das and Aki*, 1977*b*. © *Am. Geophys. Union*.)

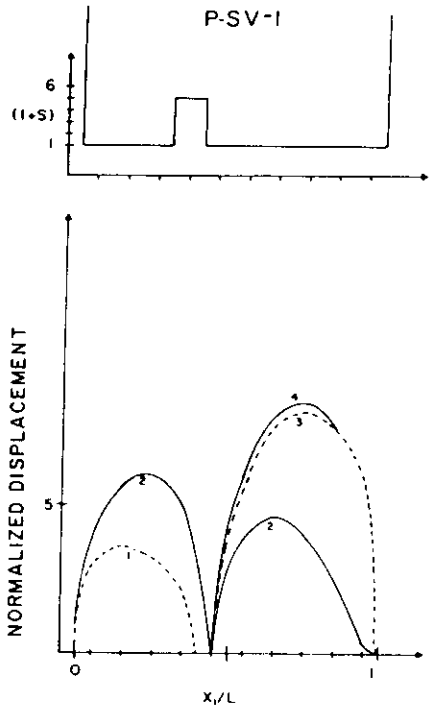

6.5 Same as Figure 6.3 but for case P-SV-1. There is now one barrier on the fault that remains unbroken at the completion of the dynamic fracture of the fault. (*From Das and Aki*, 1977*b*. © *Am. Geophys. Union*.)

limit can be obtained by comparing the numerical solution for some simple case with an analytic solution, the spectra in all the cases plotted in this example being shown only up to the frequency where the numerical results are valid) have more energy than that for the smooth fault.

7. The corner frequency averaged over all directions from the source is unaffected by the presence of unbreakable barriers.
8. The stress drop averaged over the total fault length (including the barriers) is lower for the case with unbroken barriers than the other cases. In fact, there is a stress increase on these unbroken regions due to the earthquake. Thus, a complex earthquake with lower average stress drop can generate waves of

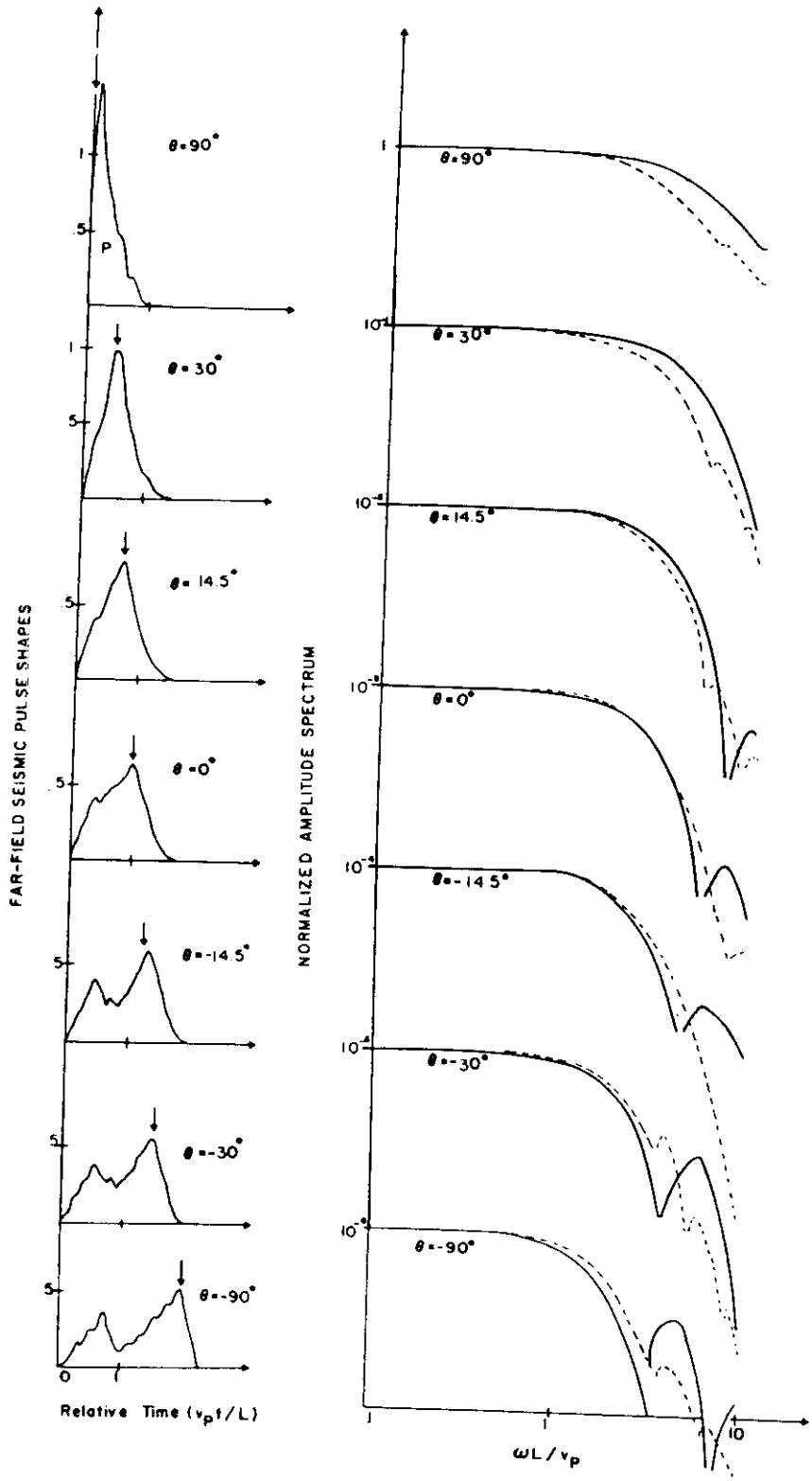

6.6 Same as Figure 6.4 but for the case P-SV-1. The dashed lines on the spectra are the curves for the case P-SV-0 and are included for the purpose of comparison. (*From Das and Aki*, 1977*b*. © *Am. Geophys. Union*.)

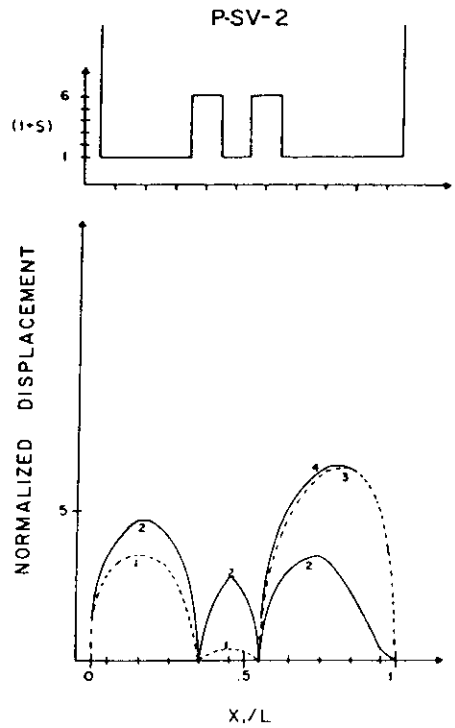

6.7 Same as Figure 6.3 but for case P-SV-2. The two barriers on the fault remain unbroken. (*From Das and Aki*, 1977*b*. © *Am. Geophys. Union*.)

relatively higher frequency than a simple earthquake with relatively higher stress drop.

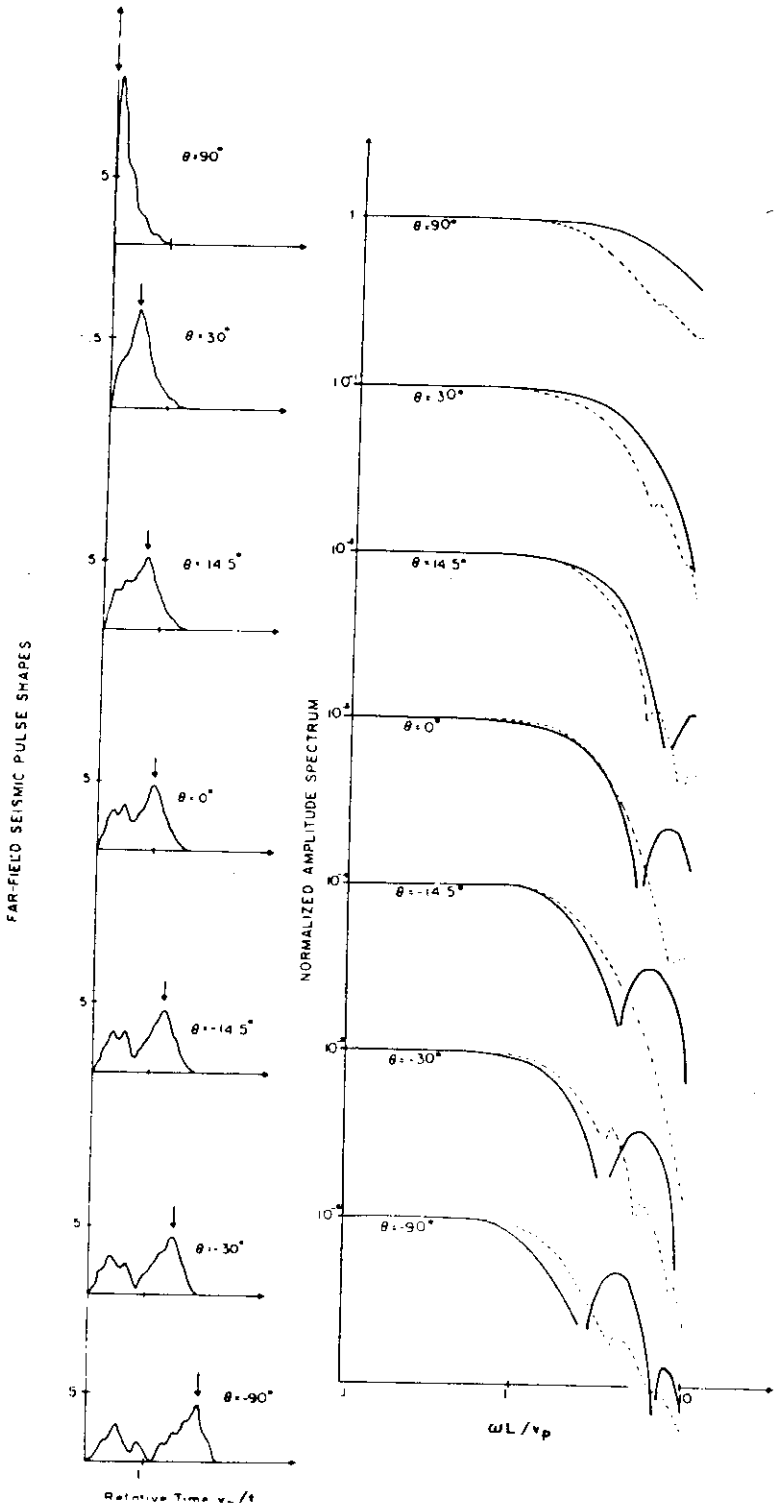

6.8 Same as Figure 6.4 but for the case P-SV-2. The dashed lines give the curve for the case P-SV-0. (*From Das and Aki*, 1977b. © *Am. Geophys. Union*.)

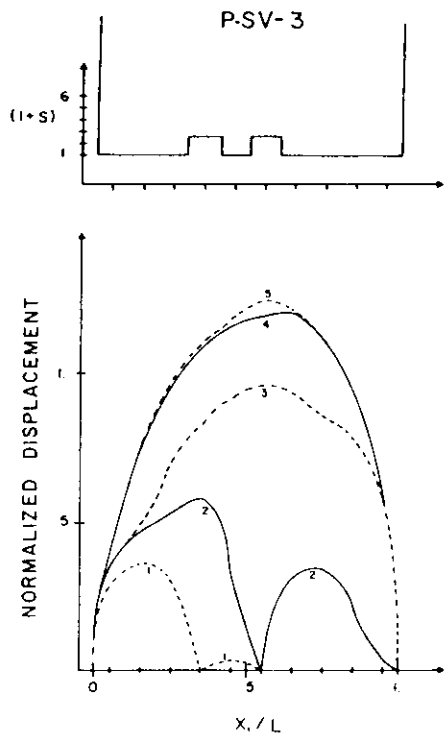

6.9 Same as Figure 6.3 but for case P-SV-3. The two barriers on the fault are of intermediate strength and eventually break while dynamic fracturing of other parts of the fault is continuing. (*From Das and Aki*, 1977*b*. © *Am. Geophys. Union*.)

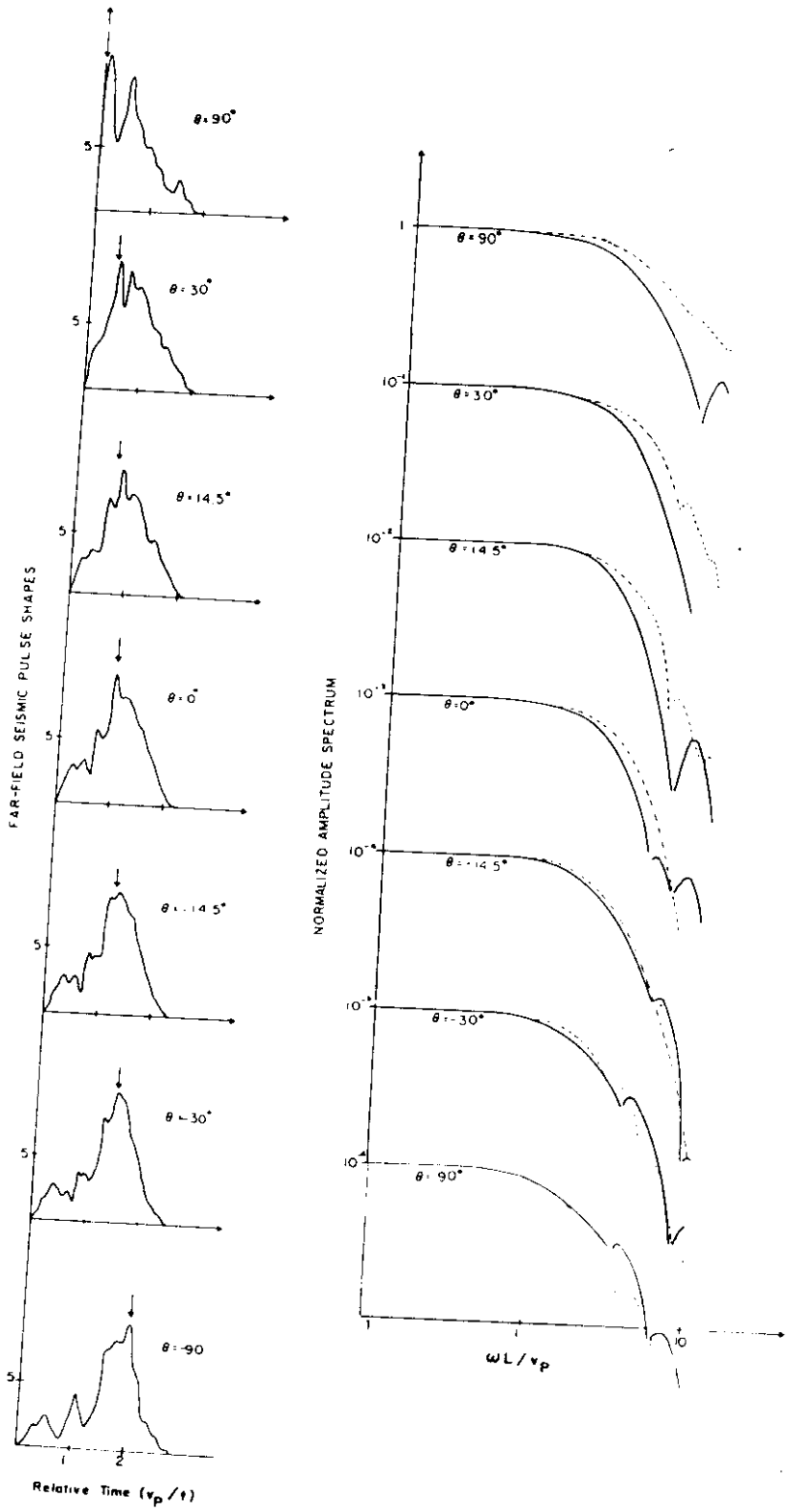

6.10 Same as Figure 6.4 but for case P-SV-3. (*From Das and Aki, 1977b. © Am. Geophys. Union.*)

The observational support for complex faulting models came from both seismology and geology. Observations of multiple shocks on seismograms were mentioned at the beginning of this section. The measured surface slip after large earthquakes often shows a form similar to the fault slip found for P-SV-1 and P-SV-2. Direct evidence from fractures on mine faces showed that faults are usually very complex, with side steps and highly deformed but unbroken ligaments in the stepover regions (Spottiswoode and McGarr, 1975; McGarr et al., 1979). The impact of this model, in spite of its idealizations, on the understanding of the earthquake faulting process was significant. It led to the characterization of barriers as being material (large S) or geometric (when the fault plane deviated from planarity) by Aki (1979). It also led to the identification of barriers in the field by structural geologists and by seismologists in various locations around the world (Lindh and Boore, 1981; King and Yielding, 1984; Nabelek and King, 1985; Sibson, 1986; Barka and Kadinsky-Cade, in press; Bruhn, Gibler, and Parry, 1987, to name only a few). Major projects are under way in many countries to identify barriers along faults and to try to understand the origin and geochemical characteristics of barriers. The primary reason for this general interest is that earthquakes often nucleate and terminate at barriers.

Since the unbroken barrier with its high residual stress concentration can become the "asperity" of a future earthquake on the same fault, it is important to consider the radiation due to the fracturing of such an unbroken barrier. In Section 5.6, we studied the dynamic fracture of isolated asperities of different shapes on infinite faults. In the next subsection, we will look at the far-field radiation generated by such a model.

Radiation due to the failure of an isolated asperity

The far-field displacement pulse shapes can be conveniently calculated for this case using (6.1.5). The corresponding radiation patterns were given in Section 4.6. Let us consider the far-field pulse shape for the circular asperity along the direction of the normal to the fault. In this direction, the P- and the S-wave pulses coincide. The pulses are given by the term

$$\sum_{i,\, j \in \Sigma_k} \tau_{\alpha i j k},$$

of (6.1.5) and plotted in Figure 6.12. The normalized time in the figure is $v_P t/\Delta X$, and it is measured from the time of arrival of the first wave at the receiver. The most striking feature of this pulse is that there is a permanent offset, in contrast to what we saw in the previous examples in

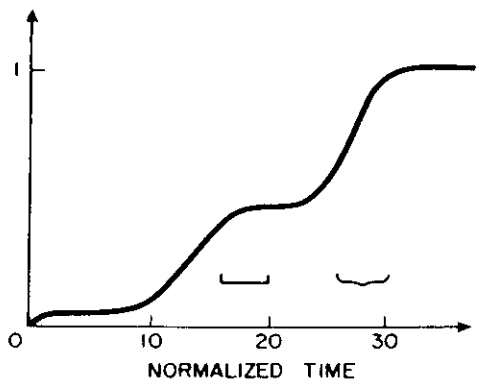

6.12 Far-field displacement pulse shape for the P and S waves along the normal to the asperity, due to the fracturing of a circular asperity (Figure 5.18). The bracket and brace are explained in the text. (*From Das and Kostrov, 1983. © Am. Geophys. Union.*)

this chapter for the conventional crack model. This is not surprising when we recall that the problem was formulated such that the two half-spaces on either side of the fault plane remain permanently shifted after the asperity has fractured and disappeared. The rise time of the displacement from zero to this final value is the time required for the asperity to fracture. The brace in the figure indicates the time when the number of grids broken per unit time is the highest. The fracture process for this case (Figure 5.18) shows that this indeed took place toward the end of the breaking process. The square bracket indicates the period when the breaking rate is high but the displacement does not increase. This is because, although the number of grids breaking per unit time is large, these points are situated far from one another on the asperity; also, they do not have large stress drops associated with them and hence do not contribute significantly to the increase in the far-field displacement. If we looked at the acceleration pulse shape (obtained simply by twice differentiating the displacement pulse in Figure 6.12), we would find that the high accelerations correspond in time to the (relative) times when the breaking rate of grids on the asperity is the highest. Thus, the far-field displacements are very sensitive to the location of fracturing points on the asperity, whereas the accelerations are sensitive to the rate of increase of the broken area but not to its distribution over the fault. The pulse shapes in other directions from the source have essentially similar characteristics, the rise times being shortest in the (general) direction of fracture propagation and longest in the opposite direction.

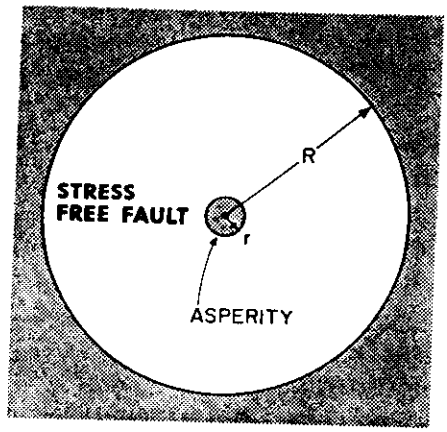

6.13 Geometry of the problem of failure of an isolated asperity on a finite fault.

The pulses for elliptical asperity fracture (Das and Kostrov, 1985) are similar and are not included here.

The asperity model

The basic idea of this model was suggested by Madariaga (1979) and by Rudnicki and Kanamori (1981). According to the model, an earthquake is caused by the failure of isolated, highly stressed regions of the fault, the rest of the fault having little or no resistance to slip (being partially broken and preslipped, say) and contributing little or no stress drop to the earthquake process. This results in a nonuniform stress drop over the fault. Since the regions without slip are able to withstand the high stresses concentrated on it until the moment the earthquake begins, it must be assumed that the parameter σ'' for these regions is higher than that for the rest of the fault. The spontaneous, dynamic fracturing of one or more such isolated asperities of general shape and size on a finite fault has not yet been studied. The simpler problem of radiation from the fracturing of a circular asperity at the center of a circular fault was studied by Das and Kostrov (1986), and we shall discuss the result here.

In this model, a circular crack of radius R, say, has a circular asperity of radius r, say, at its center (Figure 6.13). The annular region between the crack and the asperity is broken and assumed to be at or very close to the kinetic frictional level. When the central asperity breaks, this annular region exhibits no (or little) dynamic stress drop. It also has little or no resistance to slip. For the numerical calculations, r/R is taken as

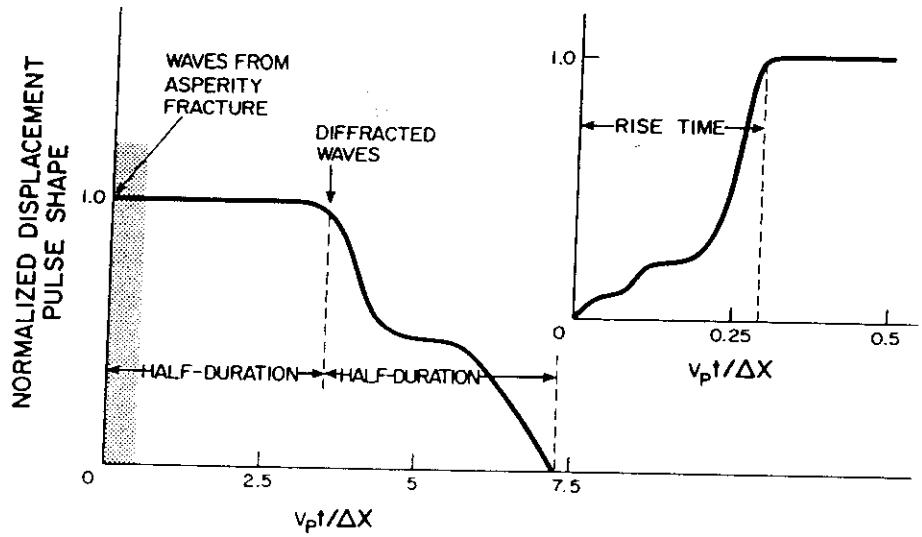

6.14 Far-field S-wave displacement pulse shape due to the failure of the isolated asperity shown in Figure 6.12. Inset shows details of pulse shape in stippled region. (*From Das and Kostrov, 1986. © Am. Geophys. Union.*)

.1 and the asperity is taken as a single spatial grid. The asperity is released, and the ensuing dynamic slip is allowed to spread out over the entire circular fault. The slip is calculated using algorithm (5.2.13) and the P- and S-wave pulse shapes in different directions from the source are found using (6.1.4). The normalized S-wave displacement pulse shape looking down at the fault along the normal as a function of normalized time $v_P t/\Delta X$ is shown in Figure 6.14 as a representative example. The displacement pulse immediately reaches its maximum value and remains flat until the first diffracted waves from the crack edge arrive at the observer at time $T_d \simeq R/v_S$, measured from the time of arrival of the first S wave. The displacement then starts decreasing and finally reaches zero at time $= 2T_d$ ($\approx 2R/v_R$). The minor oscillations following this that occur due to backslip being permitted on the fault are ignored in this figure. The duration of the flat part of the pulse is thus controlled by the size of the large crack of radius R. Since the asperity was released instantaneously in this problem, this picture does not represent the rising part of the pulse correctly. But this was calculated in the last subsection, and using those results and adjusting the time scale, we obtain the pulse shape in the stippled region of Figure 6.14, as shown in the inset of this figure. The rise time for the failure of a single asperity was shown in the

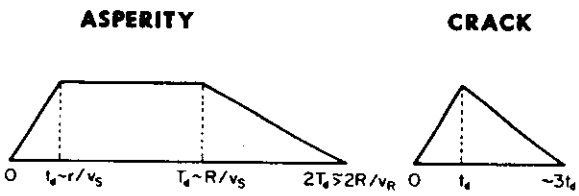

6.15 Schematic representation of the far-field displacement pulse due to the failure of an asperity on a finite fault and due to a propagating crack. (*From Das and Kostrov, 1986. © Am. Geophys. Union.*)

last subsection to be controlled by the asperity size and is given by $t_d \approx r/\beta$.

Since the details of the pulses of Figure 6.14 depend on the parameters of the particular problem (crack and asperity size and shape, fracture velocity, etc), one may neglect the details and construct a schematic representation of the pulse shape due to the fracture of an isolated asperity on a finite fault, as shown in Figure 6.15. The main features of this pulse are a steeply rising part followed by a flat portion of long duration and then a gradual return of the displacement pulse to zero. The triangular pulse from a circular crack (Figure 6.1) is also shown in the figure for comparison. If this circular crack is taken to be the same size as the asperity of the model under discussion here, then the pulse shape would have the same rise time as the asperity model. However, once the maximum amplitude is reached, the two pulses become very different in character, the crack pulse immediately starting to decrease toward zero and reaching zero at time about twice the rise time, as we saw earlier in this chapter.

Thus, the asperity pulse has an anomalously large seismic moment (area under the pulse) and anomalously large duration compared with a crack pulse for a crack of radius r. Such earthquakes have been called "slow" or "weak" earthquakes (Kanamori and Cipar, 1974; Kuznetsova et al., 1976). The spectrum of the pulse shown in Figure 6.14 was found to have the same general form as that for the conventional crack model (Figure 6.1).

It must be pointed out here that this model is not the only possible model for slow earthquakes. Clearly, such earthquakes could also be modeled as a very slowly propagating crack, due, for example, to very low stress drop.